Full length article

A low-cost experimental averaging method for fast–slow mechanical systems via long-exposure video: Application to the Kapitza pendulum

Attila Genda [ID] *, Clemens Kummer, Alexander Fidlin [ID]

Karlsruhe Institute of Technology, Kaiserstr. 12, Karlsruhe, 76131, Germany

ARTICLE INFO

ABSTRACT

Nonlinear mechanical systems are typically challenging to analyze experimentally, particularly when high-frequency motions require high temporal resolution, often making data collection difficult and expensive. This research explores an alternative approach by utilizing inexpensive and readily available long-exposure cameras, such as those found in billions of mobile devices. The method is suited to fast–slow systems in which a periodic, high-frequency motion rides on a much slower drift—examples include vibratory energy harvesters, tuned-mass dampers, and the Kapitza pendulum studied here. When the camera's exposure covers at least one fast period, pixel brightness becomes proportional to the classical probability density (CPD) of the fast motion. Substituting this CPD into the standard averaging integral yields the governing equations of the slow subsystem without resolving the high-frequency motion in time. We demonstrate the experimental feasibility of the idea on a Kapitza pendulum whose pivot vibrates at $\approx$ 48 Hz. The blurred motion of three LEDs is captured on a 30fps HD video. For each frame, the spatial average is evaluated in MATLAB®, allowing for the recovery of the slow trajectory. Consequently, a system parameter identification is performed. Furthermore, with some uncertainty, it is even possible to recover the slow system dynamics of the unexcited, physical pendulum without directly measuring it.

Long-exposure imaging thus extracts relevant slow-dynamics information with pocket-sized hardware. It eliminates the need for costly high-speed cameras, providing a practical and low-budget tool for experimental averaging and system identification.

1. Introduction

1.1. Historical development of the averaging method

The averaging method is a powerful analytical technique for systems with widely separated time scales, used to simplify the analysis of *fast oscillatory* dynamics coupled with *slow drift*. Its roots trace back to 18th-century celestial mechanics, when *Lagrange* first applied an averaging approach to the three-body problem [1]. By "averaging out" the rapid orbital perturbations (treating them as perturbations of the two-body solution), Lagrange demonstrated how one could approximate the long-term behavior of orbits. In the late 19th century, *Poincaré* extended perturbation methods for periodic celestial motions [2], laying the groundwork for rigorous averaging. The early 20th century saw *van der Pol* employ averaging to analyze periodic oscillations in radio circuits [3],

---

demonstrating the method's broad applicability beyond astronomy. A significant theoretical advance came when *Fatou* provided the first asymptotic proof of the method's validity [4], establishing conditions under which the averaged system accurately captures the long-term behavior of the original system. In the 1930s, Krylov and Bogoliubov formalized averaging for nonlinear oscillations [5], culminating in their seminal monograph on nonlinear mechanics [6]. This work established averaging as a standard tool for nonlinear vibration analysis, proving that a non-autonomous system with fast periodic forcing could be replaced by an autonomous "averaged" system for predicting slow dynamics. Subsequent influential contributions, such as *Bogoliubov* and *Mitropolsky*'s treatise on asymptotic methods [7], integrated averaging into a broader framework of perturbation techniques. A historical overview of these seminal contributions and those by *Mitropolsky* can be found in [8]. A complementary data-driven route is the *sparse identification of slow timescale dynamics*, which combines clustering, dynamic-mode decomposition, and sparse regression to infer the coarse-grained flow directly from multiscale observations without performing explicit time-domain averaging [9].

By the 1960s and 1970s, averaging had become a cornerstone of nonlinear dynamics, featured prominently in texts by *Hayashi* [10] and *Nayfeh* [11] among others [12]. These works helped disseminate multiscale methods (including averaging) to the mechanical and aerospace engineering communities [13].

1.2. Principles and modern challenges

The essence of the averaging method is to replace a fast time-varying system with an approximate system that governs the slow evolution of the *mean behavior*. Classical averaging considers a system of the form

$$\dot{x} = \varepsilon f(x,t), \tag{1}$$

(with $0 < \varepsilon \ll 1$) where $f(x,t)$ is periodic or oscillatory in t [14]. The solution $x(t)$ can be approximated by $y(t)$ solving

$$\dot{y} = \varepsilon \bar{f}(y), \tag{2}$$

where $\bar{f}(y)$ is the time-average of $f(x,t)$ over one fast oscillation [11]. This procedure results in an autonomous averaged system that "irons out" the fast oscillations yet remains close to the true dynamics over long timescales (up to $O(1/\varepsilon)$) [5]. Historically, this time averaging was performed by analytical integration over one period. However, several challenges arise in modern applications. First, many systems exhibit complex, fast dynamics (e.g., chaotic, broadband, or non-periodic oscillations), for which a simple periodic average is unavailable [15]. Second, even when the fast motion is periodic, performing time integration numerically can be computationally expensive if the timescale separation is extreme. For instance, simulating stiff mechanical systems with high-frequency components requires very short time steps, resulting in high computational costs. These issues motivate new approaches to averaging that can handle general fast motions more efficiently. One such approach is to leverage probabilistic averaging, replacing time integrals with *spatial (ensemble) cross-correlation integrals* with respect to the classical probability density (CPD) of the fast motion [16,17], even though the motion remains deterministic. The equivalence can be written as

$$\bar{f}(x_s) \;=\; \frac{1}{T}\int_0^T f\big(x_s + g(t)\big)\,\mathrm{d}t = \int_{-\infty}^{\infty} f(x)\rho(x - x_S)\mathrm{d}x \;=\; (\rho \star f)(x_s), \tag{3}$$

where

- x_s is the *slow* variable, treated as quasi-static while the fast variable cycles,
- $g(t)$ is an at least piecewise-C^1, T-periodic *fast* variable, and
- $\rho(x)$ denotes the CPD of $g(t)$.

This idea is motivated by stochastic systems and ergodic theory, where for an ergodic fast motion (i.e., its time average equals its ensemble average), one can integrate a function of the state over the stationary distribution of the fast motion instead of explicitly integrating over time, which were developed for systems with random fast fluctuations by *Stratonovich* and *Khasminskii* in the 1960s [18–20]. In the present work, we adopt a similar viewpoint: we assume the fast motion has a known CPD (either from theory or measurements), and we *substitute time integration with integration over space*, along the path of the fast variable weighted by its CPD. This substitution yields an averaged model without requiring the resolution of the fast oscillation in time. A key advantage of this CPD-based averaging is that the necessary integrals can often be evaluated analytically or very cost-effectively numerically via the FFT [16]. Compared to brute-force time simulation, this approach can be orders of magnitude faster while still capturing the correct slow dynamics. Another advantage is in *experimental identification*: the CPD of a fast motion can be empirically obtained from measurements, allowing one to construct an averaged model directly from data. In contrast, classical averaging would require identifying the precise instantaneous dynamics $f(x,t)$ and then integrating over a period—a far more challenging task if the motion is complicated or noisy. By focusing on the statistical distribution of the fast variable, the proposed approach is naturally robust to irregularities and can integrate experimental data into the analytical model.

1.3. Vision–based vibration measurement and image processing

The use of video cameras for vibration measurement has become a robust non-contact alternative to classical sensors in mechanical and civil engineering [21,22]. Modern high-speed or high-resolution cameras, combined with advanced image processing, enable engineers to capture sub-pixel motions of structures and machines from a safe distance. Each pixel effectively acts as an individual sensor, providing full-field vibration data across an object's surface [23].

Since the seminal Eulerian work of *Wu et al.* [24], research has focused on amplifying imperceptible displacements in ordinary video. A comprehensive 2024 review by *Luo et al.* surveys the state of motion-magnification (MM) techniques for civil structures and benchmarks their bandwidth and signal-to-noise characteristics [25]. Recent phase-based variants can now recover mode shapes at signal levels well below the threshold of a single pixel [26]. Deep-learning optical-flow networks further enhance accuracy: the SEA-RAFT algorithm achieves state-of-the-art flow estimation while running more than twice as fast as classic RAFT, facilitating real-time structural monitoring [27].

Full-field stereo or 3D-DIC remains the gold standard for high-fidelity displacement maps. An early benchmark study by *Beberniss & Ehrhardt* demonstrated that high-speed 3D-DIC can deliver modal surveys up to the lower-kHz range while also highlighting practical limits such as temporal aliasing and reduced out-of-plane sensitivity compared with laser vibrometry [28]. A low-speed-camera strategy introduced by *Neri et al.* (2022) exploited temporal down-sampling to measure vibrations up to 6.5 kHz with cameras running at only 10 fps [29]. Follow-up work improved sub-pixel sensitivity in 3D-DIC through spline-based correlation-map interpolation, delivering reliable kHz-bandwidth measurements on consumer hardware [30]. In 2024, the same group proposed an *Augmented-Resolution DIC* algorithm (AR-DIC) that applies quartic interpolation and local up-sampling of correlation maps to push DIC accuracy into the sub-10^{-3} px range for vibration testing [31]. These advances close the performance gap between DIC and laser vibrometry for many practical applications.

Camera-based methods now routinely capture structural responses from a few hertz to several kilohertz. Comparative studies report excellent agreement between camera-derived spectra and contact sensors, extending well into the hundreds of hertz, for bridges and machinery [21]. With AR-DIC and improved optical-flow algorithms, laboratory demonstrations have verified modal parameters at multi-kHz rates on bladed disks and cantilever beam resonators [29,30].

Where optical coherence is available, time-averaged digital holography offers a complementary route. *Hu et al.* designed a double-exposure, off-axis holographic system that records the phase-difference fringes of vibrating optical composites excited at 200–275 Hz. The spatial variation of fringe density reveals local resonance shifts, enabling the non-destructive identification of subsurface defects without the need for contact instrumentation [32].

Valente et al. present a three-stage video-analysis workflow that first employs holistically-nested edge detection to emphasize high-spatial-frequency boundaries, then amplifies their micro-motions via phase-based motion magnification, and finally tracks the magnified edges with a two-dimensional particle filter, allowing reliable non-contact extraction of structural vibration modes even under uneven lighting and partial occlusion [33].

Consequently, vision-based sensing has evolved from a proof-of-concept to a field-deployable technology in less than a decade.

1.4. Long-exposure imaging for averaging fast motion

A long-exposure photograph records the entire path of a vibrating object as a continuous streak. While the shutter is open, the sensor integrates irradiance over time, so the gray-value $I(\mathbf{s})$ at pixel $\mathbf{s}$ is proportional to the *residence time* of the object at that spatial location, i.e. to the CPD of the fast coordinate over one or more cycles [16,34]. Consequently, a single blurred frame replaces the time integral used in traditional averaging with a spatial integral that can be evaluated directly on the image. Early studies already hinted at this link: *Yitzhaky* [35] and *Sieberth* [36] analyzed blur length as a proxy for motion magnitude, and *Wang et al.* showed that geometric moments of a blurred edge yield the amplitude and direction of sinusoidal vibrations without high-speed video [37].

Recent work shifts the focus from blur *suppression* to blur *exploitation*. For qualitative diagnostics, stroboscopic and time-averaged techniques visualize mode-shape envelopes [38]. More recently, quantitative full-field methods have emerged. *McCarthy, Chandler & Palmeri* oriented multiple blurred photographs photogrammetrically and, by fitting ellipses to each streak, reconstructed the three-dimensional vibration envelope of a steel frame—detecting bolt retightening with sub-millimeter precision [39]. *Kovanič et al.* extended the idea to impact hammers and achieved trajectory errors below 1 mm from a single RGB image [40]. Complementing these still-image approaches, *Karameşe et al.* proved that even hand-held smartphone videos can deliver displacement, velocity, acceleration, and strain histories within 10–20% of reference sensors, provided that template matching and optic-flow tracking are combined judiciously [41]. At very low frequencies (1 Hz to 7 Hz) *Gong et al.* linked stripe spacing in the Fourier spectrum of a blurred cantilever directly to vibration amplitude, keeping the error below 2% [42]. Blur can also reveal unwanted *camera* motion: *Liu et al.* correlated stellar blur with micro-vibrations of a cooled CCD, showing that an internal fan degraded long-exposure sharpness and recommending water cooling instead [43]. Furthermore, blur may act as a form of compressed temporal data. *Rengarajan et al.* demonstrated that one long exposure, bracketed by two short snapshots, can be decomposed by a convolutional network into a stack of 20–40 sharp intermediate frames, effectively "unrolling" the blur into time-resolved imagery [44].

The concept of obtaining CPD from an image is straightforward. Because intensity is proportional to occupancy time, and camera sensors integrate incident light during exposure time, pixel brightness values are proportional to the light source's dwell time at a given pixel, yielding the CPD of the fast motion. Inserting this CPD into the averaging integral (3) gives the slow drift without resolving the rapid oscillation in time. A single photograph thus bridges the gap between experiment and theory. Practically, any modern smartphone or even a cheap Raspberry Pi camera can capture valid CPD data. Depending on bandwidth constraints, this offers a continuum between static CPD-based averaging and full high-fps video reconstruction. In summary, long-exposure imaging transforms motion blur from a nuisance into a low-cost, high-bandwidth sensor that underpins experimental averaging of fast–slow mechanical systems.

In practice, successful blur-based averaging requires that the exposure covers at least one complete vibration period to guarantee a stationary CPD, that the scene has sufficient contrast (or artificial targets) for reliable streak segmentation, and that internal camera shake is negligible compared with the object motion. When these conditions hold, the blur envelope serves as an instantaneous
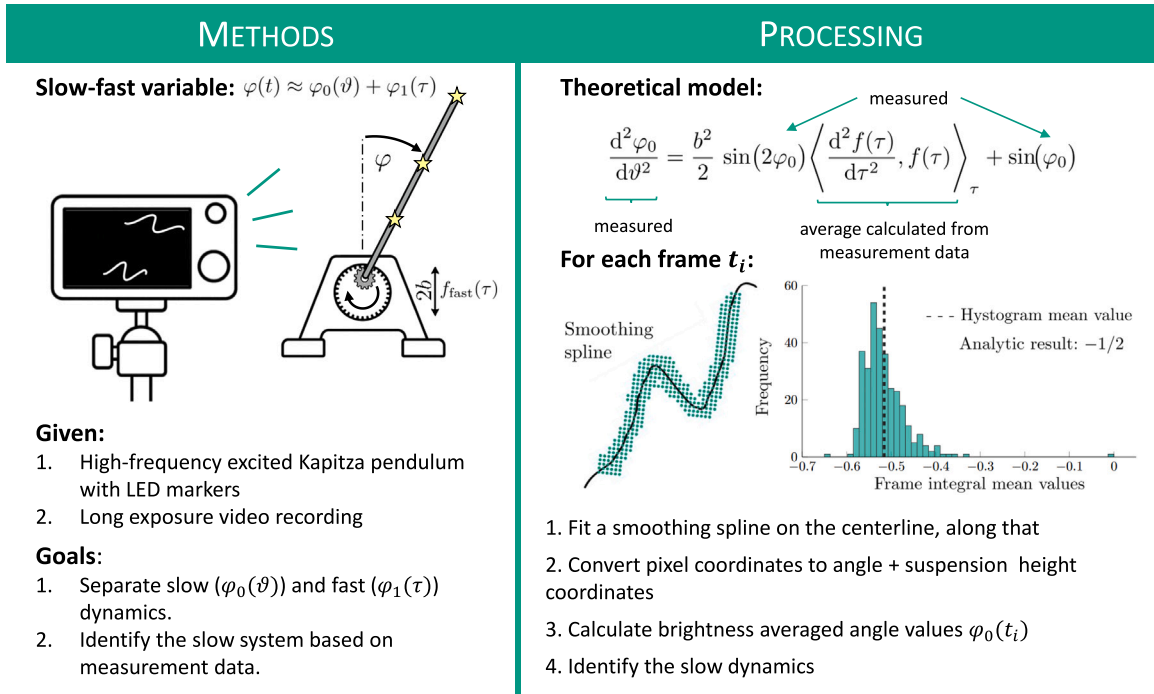
Fig. 1. The applied measurement methods and processes.

experimental surrogate for the time average, allowing for model reduction of fast–slow mechanical systems without the storage burdens associated with high-speed video. Even a basic Raspberry Pi camera is sufficient for tabletop resonators. This measurement setup also has the potential for real-time measurement evaluation, system monitoring, and identification (see Fig. 1).

This paper is structured as follows. In Section 2, the experimental and measurement setup is described. In Section 3, the corresponding mechanical model is described, and the slow flow equations are derived analytically. In Section 4, the image processing algorithm is described, followed by Section 5 discussing the results. Finally, Section 6 gives a summary and scope for future research.

2. Experimental setup and measurement method

2.1. Mechanical system

The experimental apparatus is a physical pendulum with a vibrating suspension point — a classic teaching experiment designed to illustrate nonlinear oscillatory effects [45–49].

An unexcited pendulum is known to have two equilibrium positions: an unstable equilibrium when it is vertically upward and a stable equilibrium when it is vertically downward. A sufficiently fast vertical vibration of the suspension point stabilizes the upper equilibrium [50]. Consequently, in addition to the typical oscillation about the lower equilibrium, an oscillation about the upper "equilibrium" can also be observed. Although the pendulum is continuously in motion, the term "equilibrium" is used because the human eye processes only the slow pendulum motion rather than the rapid vibration. A sufficiently fast vibration with a horizontal component shifts these two equilibria in the direction of the vibration; under high-frequency horizontal vibration, the equilibria are located to the right and left of the suspension point.

An overview of the experimental setup is shown in Fig. 2. A pendulum is attached via a ball bearing to a vibrating suspension so that it can freely rotate about the suspension point. Fig. 3 shows a close-up of the suspension without the pendulum. A planetary gearbox converts the motor's rotation into vibration with an adjustable direction; one motor revolution corresponds to one period of the vibration. The rotation frequency of the motor is set to approximately 48 Hz. This frequency is high enough that the human eye cannot resolve the vibration, so the pendulum appears as a blurred object.

The relevant system dimensions were measured and are listed in Table 1. A technical drawing is available here.
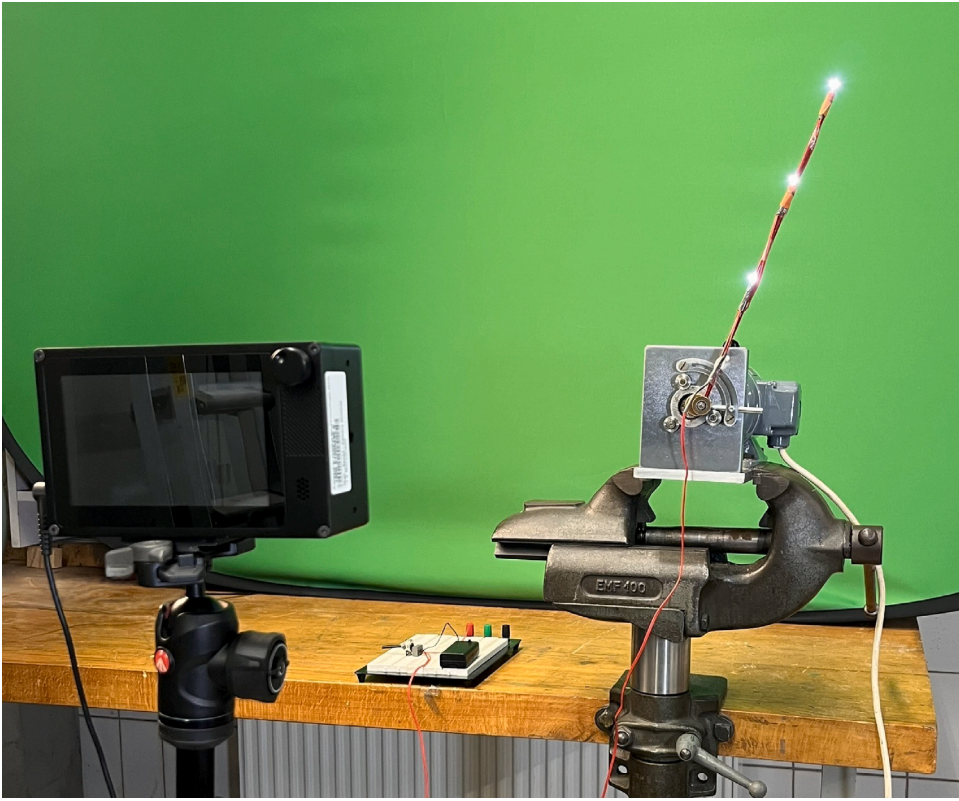
Fig. 2. Overview of the entire experimental setup, including the pendulum attached to an electric motor providing harmonic excitation; three white LEDs with adjustable brightness and their power supply; a camera.
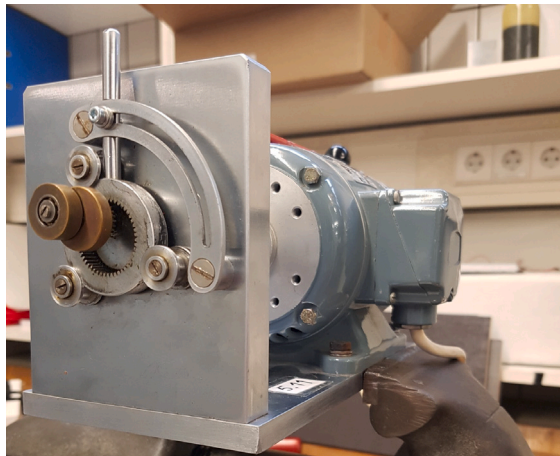

Fig. 3. Close-up of the motor with gearbox.

2.2. Marking

Three LEDs are attached to the pendulum to visualize its motion (see Fig. 2). They are powered by a 3 V battery connected with an electric wire, with a potentiometer connected in between to adjust the brightness of the LEDs, which are precisely dimmed to avoid overexposure in the recordings.

Since the LEDs are light sources, they appear much brighter than any other object in the background. Thus, no specific background is needed; it is only necessary that the room is sufficiently dark to appear black in the video. This way, only the

Table 1

Dimensions of the system.

Quantity	Symbol	Measurement
Rod length	l_{Rod}	30.1 cm
Rod diameter (with LED)	d_{Rod}	5 mm
Rod mass	m_{Rod}	23 g
Outer diameter of ball bearing	$2R_{\mathrm{a}}$	18 mm
Inner diameter of ball bearing	$2R_{\mathrm{i}}$	5 mm
Width of ball bearing	b_{BB}	6 mm
Ball bearing mass	m_{BB}	10 g
Distance from suspension point to LED	$R_{\mathrm{LED,1}}$	31 cm
	$R_{\mathrm{LED,2}}$	22.1 cm
	$R_{\mathrm{LED,3}}$	12.7 cm
Stroke (double amplitude)	$2|\vec{a}|$	24.4 mm

LEDs are visible, and their image can be directly processed. Due to the wire, the pendulum cannot rotate in 360° and the wire may also introduce a slight damping and stiffening effect. The mass of the LEDs is negligible in the calculations.

2.3. Recording with a digital camera

Measurements are performed using video recordings. A conventional digital camera (Canon PowerShot G7 X) with adjustable exposure time is employed. The camera is placed facing perpendicular to the oscillation plane of the pendulum, with its sensor collinear to the electromotor's axis. The distance and zoom of the camera are chosen such that the oscillating LEDs occupy most of the image, but distortion to the perspective remains negligible. The video resolution is chosen to be 30 fps, which allows the fast oscillation to complete a whole period on each frame. The exposure time is set to be maximal, i.e., approximately 1/30 s, so that the fraction of the frame duration that cannot be recorded, i.e., the reset time of the sensor, is minimal. The ISO values are carefully set to prevent the maximum recorded light intensity from saturating the image. To ensure a linear relationship between pixel brightness and the total amount of incident light (see Section 2.4), ISO values are chosen such that the maximum brightness remains below 140 (out of 255). Apart from the ISO value setting, the LEDs' brightness is also controllable by a potentiometer, ensuring that even with a bright background, the experiment can be performed well, without disturbing background noise. In such cases, a very low ISO value and ample LED brightness are chosen.

The video displays a blurred, bright trajectory against a black background when the pendulum is in motion. The light intensity reflects the probability of an LED being at a given position.

The basic idea of the measurement method is that an LED emits light continuously over time. The exposure time, also called shutter speed, is the length of time the shutter remains open, during which the sensor collects incoming light. During this period, the sensor records the amount of light arriving from all directions in the camera's field of view. However, no information is available regarding the exact timing of the light reception or the precise moment when the LED was at a particular location. Therefore, a single frame of the video contains only information about the probability of the LED being at a specific position.

Other important parameters for the video recordings are resolution and frame rate. The resolution (expressed in pixels as width × height) indicates the sensor's spatial discretization, while the frame rate (measured in fps) indicates how many images per second are captured. Fig. 4(a) shows an example frame. In the blurred path representing the moving LED, significant brightness variations are visible; the turning points of the path appear distinctly brighter, indicating that the LED moves more slowly there.

The Canon PowerShot G7 X can record videos up to Full HD (1920 × 1080) at 60 fps. For the analysis, each frame must capture at least one period of the vibration (approximately 48 Hz); thus, a frame rate of 30 fps is appropriate. The chosen resolution is HD (1280 × 720), which is sufficient to capture the pendulum's motion accurately. The video was recorded in .MP4 format with lossy compression, which may introduce slight data loss. Individual frames were extracted in MATLAB®, storing brightness as 8-bit intensity values from 0 to 255. The camera sensor is a BSI-CMOS sensor that employs a rolling shutter, meaning the pixels are read sequentially from top to bottom rather than simultaneously. As a result, the lower rows of pixels are captured later than the upper rows within each frame, a phenomenon also observable in the analyzed recordings. While the three LEDs on the pendulum vibrate in phase, a noticeable phase shift between the upper and lower LEDs can be observed in individual frames (see 4(a)). However, this does not adversely affect the measurements compared to using a global shutter camera, as the rolling shutter speed exceeds the maximum speed of the light sources. Therefore, once the rolling shutter reaches the position of an LED in the image, its entire consecutive trajectory for the frame will be recorded. The LED cannot catch up to the shutter, and therefore, segments of its trajectory cannot disappear from the frame. Since the camera is not moving, and the LEDs are practically point light sources, no other rolling shutter effects could arise apart from the one discussed above. Furthermore, there is a discrepancy between the frame rate and actual exposure times. In Fig. 4(b), two consecutive frames (overlaid in different colors) show a black gap between the blurred trajectories of the LED, indicating a brief period during which the camera does not record due to the sensor's readout and reset times; before a pixel can be exposed again, it must be briefly reinitialized. For the graphical discussion of the rolling shutter effect and the occurring gap between frames, see Fig. 5.
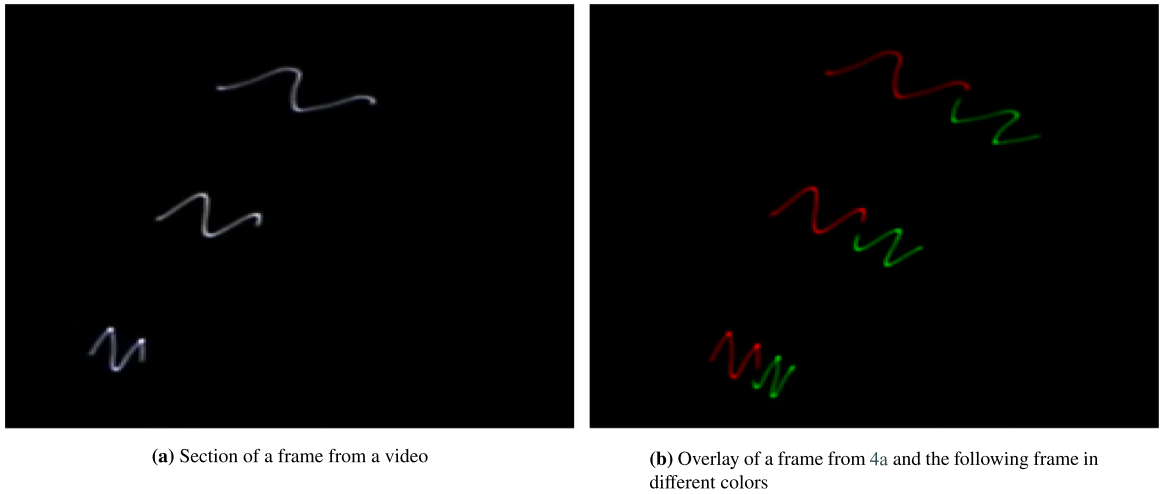
(a) Section of a frame from a video

(b) Overlay of a frame from 4a and the following frame in different colors

Fig. 4. Examples of light strokes on a single frame and on two consecutive frames.
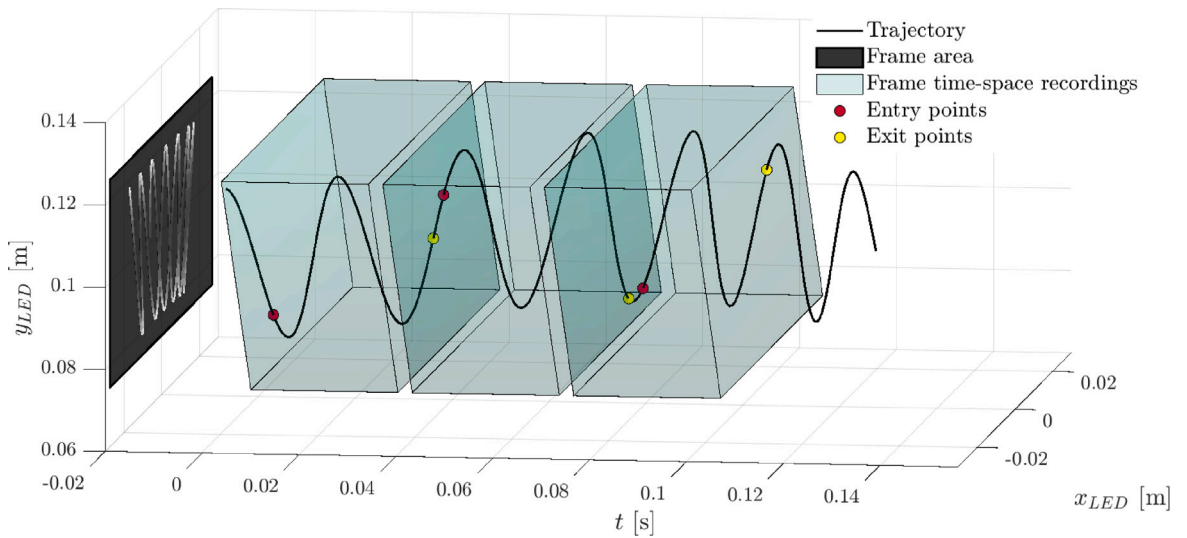

Fig. 5. The effects of rolling shutter. The reset pointer starts integration, and the readout pointer follows nearly in 1/30 s distance. The pointers proceed at a constant speed from the top to the bottom of the image, repeating the process for each frame. For every pixel, all incident light is integrated during the time between the passage of the two pointers. Due to this, the recorded slice of the time-space volume is not a cuboid, but a parallelepiped (a simplification smoothing out the rugged, step-wise boundary, due to the finite number of lines). Since the reset and readout time cannot be zero, an unrecorded gap always remains. With the applied settings, the pointers' vertical speed was always larger than the LEDs' vertical speed, a LED will enter and exit a parallelepiped only once, ensuring that the rolling shutter does not add any artifact to the recording.

2.4. Accounting for gamma correction

In imaging systems, gamma correction is standard due to the nonlinear relationship between recorded light and perceived brightness [51]. The output intensity typically follows

$$I_{\text{out}} = I_{\text{in}}^{\gamma}, \quad \gamma \approx 2.2. \tag{4}$$

Digital cameras apply an inverse gamma correction

$$I = I_0^{\frac{1}{\gamma}}, \tag{5}$$

where $I_0 \in [0, 1]$ is the sensor-recorded light. This transformation steepens the slope at low intensities, potentially amplifying noise. Consequently, many cameras employ a piecewise function: linear at low brightness levels and gamma-corrected for higher intensities.
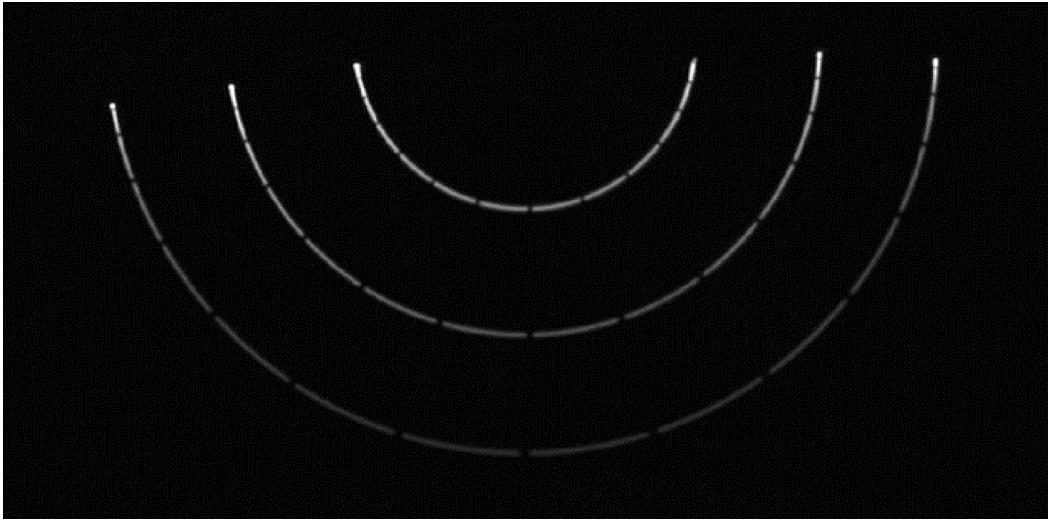
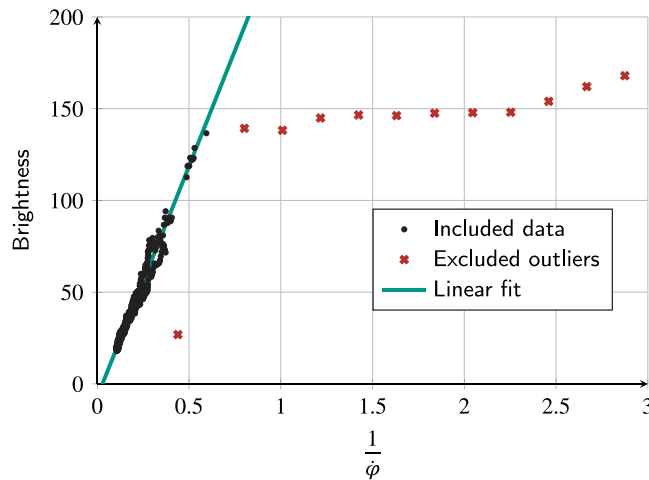**Fig. 6.** Half oscillation of the undamped pendulum to determine the brightness-velocity relationship.

Fig. 7. Angular velocity dependence of pixel brightness evaluated along the first half oscillation of the pendulum. Up to a value of 140, the brightness changes linearly with the angular velocity's inverse.

Determining the CPD from the video data requires knowledge of the camera's gamma function. Because no manufacturer data were available, the camera's response was estimated experimentally. The unexcited pendulum was released from the horizontal position, and the free oscillations were recorded (see Fig. 6). For every frame, a corresponding mean angle φ can be determined, from which the angular velocity $\dot{\varphi}$ can be inferred by numerical differentiation. Finally, the recorded brightness $B(\dot{\varphi}(\varphi))$ can be plotted against $1/\dot{\varphi}(\varphi)$. A linear approximation proved sufficiently accurate in the intensity range of interest (see Fig. 7). The linear fit

$$B = \frac{c_1}{\dot{\varphi}} + c_2 \tag{6}$$

yields $c_1 = 251.58 \pm 0.28$ and $c_2 = -7.10 \pm 0.05$ with an R^2 value of 0.9996. Thus, in the measured brightness range of 20–140, the assumption of inverse proportionality between velocity and brightness is justified.

3. Mechanical setup

The mechanical system (see Fig. 8) is a pendulum composed of a rod and a ball bearing. The center of mass $S = (x_S, y_S)$ is given by its coordinates, and the angle φ between the vertical and the pendulum is the sole degree of freedom. The gravitational acceleration g acts in the negative y direction. The suspension point A oscillates about the origin O, with the amplitude represented
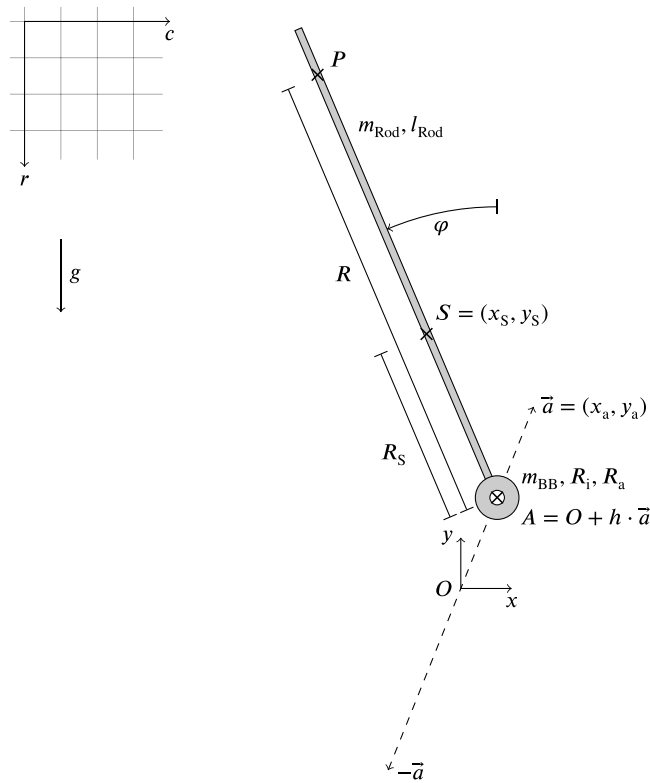
Fig. 8. Sketch of the pendulum with the relevant definitions.

by the vector $\bar{a}$ from O to the upper turning point. The dimensionless coordinate h describes the position of A along $\bar{a}$ (with $h = 1$ corresponding to the upper turning point and $h = -1$ to the lower one). The oscillation in h is given by the periodic function

$$h = f(\Omega t) \in [-1, 1] \quad \text{with period} \quad T = \frac{2\pi}{\Omega}, \tag{7}$$

and the excitation is high-frequency, i.e., $\Omega \gg 1$. The coordinate system (r, c) refers to the pixels in a frame (with r denoting the row and c the column).

3.1. Equation of motion

We derive the equation of motion using the Euler–Lagrange formalism. The kinetic energy is

$$E_{\text{kin}} = \frac{1}{2} m_{\text{tot}} (\dot{x}_S{}^2 + \dot{y}_S{}^2) + \frac{1}{2} J_S \dot{\varphi}^2 \tag{8}$$

and the potential energy is

$$E_{\text{pot}} = m_{\text{tot}} \, g \, y_S \,. \tag{9}$$

To obtain an equation for the single degree of freedom φ, the position of the center of mass is expressed as

$$x_S = h \, x_a - R_S \sin \varphi \,, \tag{10}$$

$$y_S = h \, y_a + R_S \cos \varphi \,. \tag{11}$$

Their time derivatives are

$$\dot{x}_S = \dot{h} \, x_a - \dot{\varphi} \, R_S \cos \varphi \,, \tag{12}$$

$$\dot{y}_S = \dot{h} \, y_a - \dot{\varphi} \, R_S \sin \varphi \,. \tag{13}$$

Here, the total mass m_{tot}, the moment of inertia about the center of mass J_S, and the distance R_S (from A to S) are assumed known (cf. Table 1) or determined from video data. Although the damping is small, it is included via the damping constant d. The Euler–Lagrange equation for φ reads

$$\frac{\text{d}}{\text{d}t} \left(\frac{\partial E_{\text{kin}}}{\partial \dot{\varphi}} \right) - \frac{\partial E_{\text{kin}}}{\partial \varphi} + \frac{\partial E_{\text{pot}}}{\partial \varphi} = -d \, \dot{\varphi} \,. \tag{14}$$

leading to the equation of motion

$$\left(m_{\text{tot}}\, R_{\text{S}}^2 + J_{\text{S}}\right)\ddot{\varphi} = m_{\text{tot}}\, R_{\text{S}}\, \ddot{h}\, \left(x_{\text{a}} \cos\varphi + y_{\text{a}} \sin\varphi\right) + m_{\text{tot}}\, R_{\text{S}}\, g\, \sin\varphi - d\, \dot{\varphi}\,. \tag{15}$$

3.2. Approximation via the multiple-scales method

Due to the nonlinearity of the differential equation, an exact analytical solution is not possible. Instead, an approximate solution is obtained using the multiple-scales method. To distinguish between the fast and slow subsystems, two independent dimensionless time variables are introduced. The dimensionless slow time $\vartheta = \Omega_0 t$, and the dimensionless fast time $\tau = \Omega t$.

Here, Ω is the angular frequency of the high-frequency excitation $f(\Omega t)$, while the slow time scale is set by the resonance frequency of the unexcited pendulum

$$\Omega_0 = \sqrt{\frac{g}{R_{\text{S}} + \frac{J_{\text{S}}}{m_{\text{tot}} R_{\text{S}}}}}\,. \tag{16}$$

Since $\Omega \gg \Omega_0$, τ evolves much faster than ϑ. Thus, τ is the "fast time" and ϑ is the "slow time".

Time derivatives transform as

$$(\dot{\ldots}) = \frac{\mathrm{d}}{\mathrm{d}t}(\ldots) = \Omega_0 \frac{\partial(\ldots)}{\partial\vartheta} + \Omega \frac{\partial(\ldots)}{\partial\tau}\,, \tag{17}$$

$$(\ddot{\ldots}) = \frac{\mathrm{d}^2}{\mathrm{d}t^2}(\ldots) = \Omega_0^2 \frac{\partial^2(\ldots)}{\partial\vartheta^2} + 2\Omega_0\Omega \frac{\partial^2(\ldots)}{\partial\vartheta\partial\tau} + \Omega^2 \frac{\partial^2(\ldots)}{\partial\tau^2}\,. \tag{18}$$

Since the excitation is given by

$$h = f(\Omega t) = f(\tau)\,, \tag{19}$$

its second derivative becomes

$$\ddot{h} = \Omega^2 \frac{\mathrm{d}^2 f(\tau)}{\mathrm{d}\tau^2}\,. \tag{20}$$

Inserting these into Eq. (15) and introducing the dimensionless parameter

$$\omega = \frac{\Omega}{\Omega_0} \gg 1\,, \tag{21}$$

as well as

$$a = \frac{x_{\text{a}}}{R_{\text{S}} + \frac{J_{\text{S}}}{m_{\text{tot}} R_{\text{S}}}}\omega, \quad b = \frac{y_{\text{a}}}{R_{\text{S}} + \frac{J_{\text{S}}}{m_{\text{tot}} R_{\text{S}}}}\omega, \quad \delta = \frac{1}{\Omega_0}\frac{d}{m_{\text{tot}} R_{\text{S}}^2 + J_{\text{S}}}\,, \tag{22}$$

the dimensionless form of the equation of motion becomes

$$\frac{\partial^2\varphi}{\partial\vartheta^2} + 2\omega \frac{\partial^2\varphi}{\partial\vartheta\partial\tau} + \omega^2 \frac{\partial^2\varphi}{\partial\tau^2} = \omega \frac{\mathrm{d}^2 f(\tau)}{\mathrm{d}\tau^2}\left(a\cos\varphi + b\sin\varphi\right) + \sin\varphi - \delta\left(\frac{\partial\varphi}{\partial\vartheta} + \omega\frac{\partial\varphi}{\partial\tau}\right). \tag{23}$$

The asymptotic expansion and the subsequent averaging that reduce Eq. (23) to a slow-flow equation are carried out in Appendix A, yielding

$$\frac{\mathrm{d}^2\varphi_0}{\mathrm{d}\vartheta^2} = \left[\frac{b^2 - a^2}{2}\sin 2\varphi_0 + ab\cos 2\varphi_0\right]\left\langle \frac{\mathrm{d}^2 f(\tau)}{\mathrm{d}\tau^2} f(\tau)\right\rangle_\tau + \sin\varphi_0\,, \tag{24}$$

which can be reformulated in a video data-compatible form as

$$\frac{\mathrm{d}^2\varphi_0}{\mathrm{d}\vartheta^2} = -\left(\frac{b^2 - a^2}{2}\sin 2\varphi_0 + ab\cos 2\varphi_0\right)\frac{1}{4\pi^2}\int_{s_1}^{s_2}\left(\frac{\mathrm{d}h}{\mathrm{d}s}\right)^2 \frac{1}{\rho_T(s)}\,\mathrm{d}s + \sin\varphi_0\,, \tag{25}$$

where s denotes the arc length of the motion's trajectory and $\rho_T(s)$ is the CPD determined from the brightness along the trajectory. For details of the derivation, see Appendix B.

3.3. Formulation of the potentials

Since the vibration-induced term in Eq. (25) depends only on φ_0 (and not on its time derivatives), it is convenient to define a vibration-induced potential U_{V} in addition to the unexcited system's potential U_0, which here is the gravitational potential. The terms in Eq. (25) correspond to (dimensionless) accelerations that are the negatives of the derivatives of the potentials with respect to φ_0:

$$U_{\text{V}}'(\varphi_0) = \frac{\mathrm{d}U_{\text{V}}}{\mathrm{d}\varphi_0} = -\left(\frac{b^2 - a^2}{2}\sin 2\varphi_0 + ab\cos 2\varphi_0\right)\left\langle \frac{\mathrm{d}^2 f(\tau)}{\mathrm{d}\tau^2} f(\tau)\right\rangle_\tau\,, \tag{26}$$

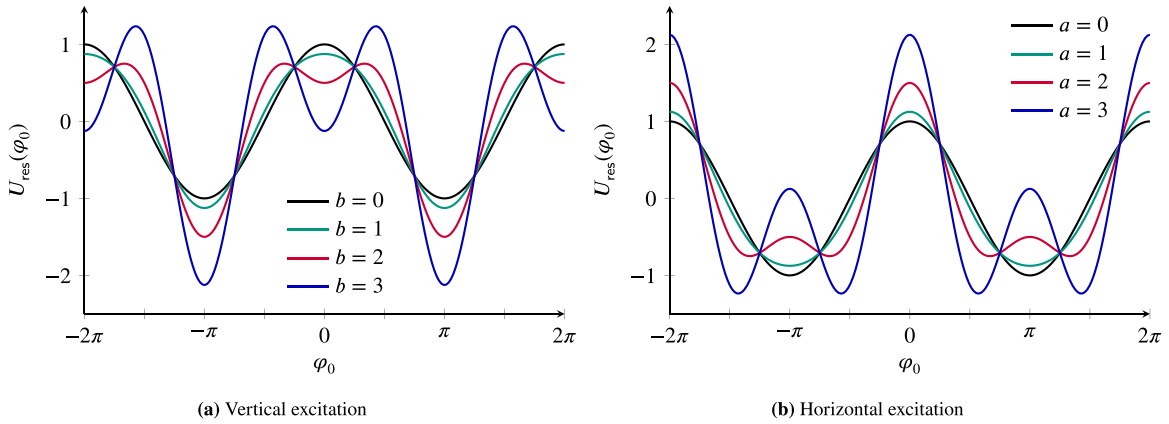**(a)** Vertical excitation

(b) Horizontal excitation

Fig. 9. Resulting potential for horizontal excitation ($b = 0$) and vertical excitation ($a = 0$) with varying strength.

$$U_0'(\varphi_0) = \frac{\mathrm{d}U_0}{\mathrm{d}\varphi_0} = -\sin\varphi_0 \,. \tag{27}$$

After integration (neglecting constants), the potentials become

$$U_\mathrm{V}(\varphi_0) = \left(\frac{b^2 - a^2}{4} \cos 2\varphi_0 - \frac{ab}{2} \sin 2\varphi_0 \right) \left\langle \frac{\mathrm{d}^2 f(\tau)}{\mathrm{d}\tau^2} f(\tau) \right\rangle_\tau, \tag{28}$$

$$U_0(\varphi_0) = \cos\varphi_0 \,. \tag{29}$$

The total dimensionless force is then given by

$$U_\mathrm{res}'(\varphi_0) = \frac{\mathrm{d}^2\varphi_0}{\mathrm{d}\vartheta^2} = U_\mathrm{V}'(\varphi_0) + U_0'(\varphi_0), \tag{30}$$

so that upon integration, the total dimensionless potential is

$$U_\mathrm{res}(\varphi_0) = U_\mathrm{V}(\varphi_0) + U_0(\varphi_0) \,. \tag{31}$$

For example, if a sinusoidal excitation is chosen, i.e.,

$$\left\langle \frac{\mathrm{d}^2 \sin\tau}{\mathrm{d}\tau^2} \sin\tau \right\rangle_\tau = \left\langle -\sin^2\tau \right\rangle_\tau = -\frac{1}{2} \,, \tag{32}$$

then according to Eq. (22) a purely vertical excitation corresponds to $a = 0$, while a purely horizontal one has $b = 0$. Fig. 9 illustrates the effects of these specific excitations. A vertical excitation (with sufficiently large b) stabilizes the upper equilibrium at $\varphi_0 = 0$ and the lower equilibrium at $\varphi_0 = \pm\pi$, whereas a horizontal excitation destabilizes the latter and creates two new equilibria approaching $\varphi_0 = \pm\frac{\pi}{2}$.

If the slow motion φ_0 and the vibration-induced potential U_V are known, the unexcited potential can also be determined via

$$U_0(\varphi_0) = \int \frac{\mathrm{d}^2\varphi_0}{\mathrm{d}\vartheta^2} \,\mathrm{d}\varphi_0 - U_\mathrm{V}(\varphi_0) \,. \tag{33}$$

This formulation allows one to generalize the approach and, by incorporating video data, even treat U_0 as an unknown to be determined experimentally. In the following, the objective is to determine integral (32) as well as $U_\mathrm{res}(\varphi_0)$ and $U_0(\varphi_0)$ from Eqs. (31) and (33).

4. Analysis of video data

To compute the vibration-induced potential from Eq. (28), all unknown parameters must be determined. The vibration-induced force is derivable solely from the video data in a simpler, rod-only system (with a massless bearing). However, for the present system, measured quantities from Table 1 are required (see Section 4.7) to determine the moment of inertia J_S, the total mass m_tot, and the center of mass r_S. The remaining parameters are extracted from the video by analyzing the LED's trajectory over one oscillation period. The brightness values along this path provide an approximation of the CPD $\rho_\mathrm{T}(s)$. A coordinate transformation is then applied to obtain the location of the suspension point h and an estimate of the slow motion φ_0, using the origin, the oscillation amplitude, and the LED position R on the pendulum. Additionally, the excitation frequency Ω is determined from the video. This section outlines the numerical procedures used to obtain these quantities and their MATLAB® implementation.
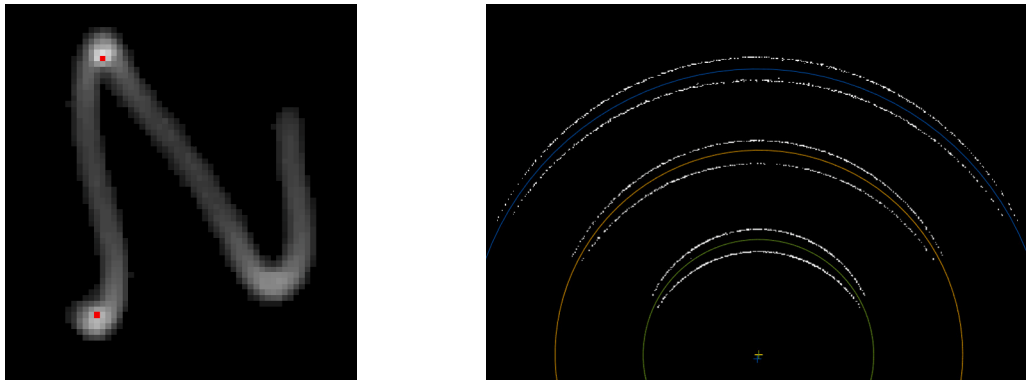
(a) Excerpt of a frame displaying the path of the LED and red-marked intensity maxima of its brightness along the path

(b) Accumulated brightness maxima from individual frames with circles that separate the lower from the upper maxima

Fig. 10. Example of an LED trajectory on a single frame and its accumulated brightness maxima across all frames.

4.1. Origin, amplitude, and position of the LED

To convert the original video coordinates (r, c) into φ and h (see Section 4.2), the turning points of each LED are identified in every frame. These turning points occur when the coordinate h, or equivalently the function $f(\Omega t)$, reaches its maximum (value 1) and minimum (value -1).

Each color frame is first converted to grayscale. To suppress background noise, pixels with intensities below $I = 5$ are set to black. The blurred trajectories of the three LEDs are then identified as connected regions using MATLAB®'s `bwconncomp`. In the experiment, turning points are defined as pixels with maximal intensity. Since the exposure time slightly exceeds one period, each frame contains two or three turning points; hence, the two brightest maxima per LED are selected. Fig. 10(a) illustrates a frame with the two detected extrema marked in red.

The accumulated maxima yield a composite image showing two circular arcs for each LED. The arcs have equal radii as the LEDs are rigidly fixed on the pendulum at a constant distance R. Their centers correspond to the turning points of the vibration, and the origin is the midpoint between them.

For each LED, a circle is first fitted to separate the data of lower turning points from the upper ones, as shown in Fig. 10(b). The circles are computed by minimizing the squared residuals between the accumulated maxima and the circles with unknown center coordinates (r, c) and radii, respectively. An initial guess with the center at the middle of the lower image border and a radius equal to half the image height yields reliable results.

In the next step, the six circles and their centers are fitted. The upper turning points for all three LEDs share the same center, as do the lower turning points, respectively. The resulting objective function involves three unknown radii and four center coordinates. From the centers corresponding to the suspension points A_{t} and A_{b}, the origin and the amplitude vector are computed in the (r, c) coordinate system as

$$\vec{a}_{\text{rc}} = \frac{1}{2}\left(A_{\text{t},rc} - A_{\text{b},rc}\right), \tag{34}$$

$$O_{\text{rc}} = A_{\text{b},rc} + \vec{a}_{\text{rc}}. \tag{35}$$

Fig. 11 displays the six fitted circles representing the turning positions of the suspension points A_o and A_u, as well as the computed origin O.

4.2. Coordinate transformation

A point on the pendulum at a fixed distance R from the suspension point (see Fig. 8) can be uniquely represented in the image plane by the coordinates h and φ. Although the mapping becomes ambiguous for pendulum positions perpendicular to the amplitude, such cases do not occur in the present videos. The position of P_{LED} (see Fig. 8) in (r, c) coordinates is given by

$$r_{P_{\text{LED}}} = r_O + h\, r_{\text{a}} - R_{\text{LED}} \cos\varphi, \tag{36}$$

$$c_{P_{\text{LED}}} = c_O + h\, c_{\text{a}} - R_{\text{LED}} \sin\varphi, \tag{37}$$

where $O = (r_O, c_O)$ is the origin, $P_{\text{LED}} = (r_P, c_P)$, $\vec{a} = (r_{\text{a}}, c_{\text{a}})$ is the amplitude vector, and R_{LED} is the distance from the suspension point to P_{LED}. From Eq. (37) one obtains

$$\varphi = -\arcsin\left(\frac{c_P - c_O - h\, c_{\text{a}}}{R_{\text{LED}}}\right), \quad \varphi \in \left[-\frac{\pi}{2}, \frac{\pi}{2}\right]. \tag{38}$$
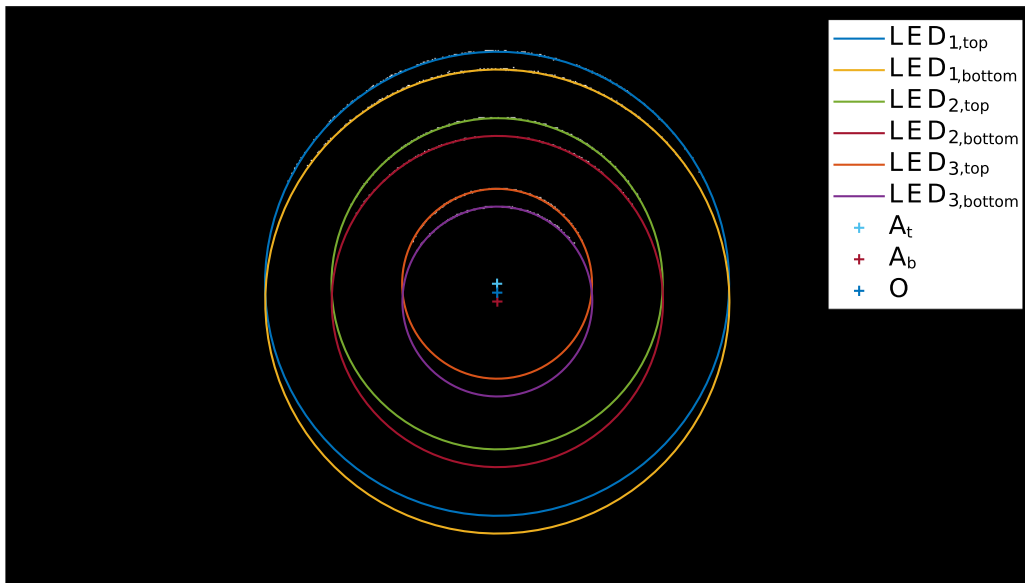
Fig. 11. Accumulated maxima from individual frames with circles delineating the motion radius of the LED.

Since only the upper half of the possible positions is recorded, φ is restricted to $\left[-\frac{\pi}{2}, \frac{\pi}{2}\right]$. For this range, Eq. (36) can be rearranged as

$$r_O + h\, r_a - r_P = R_{LED} \sqrt{1 - \sin^2 \varphi}\,. \tag{39}$$

Substituting Eq. (38) and completing the square leads to

$$h = -K \pm \sqrt{L + K^2}\,, \tag{40}$$

with the auxiliary quantities

$$K = \frac{(r_O - r_P)r_a + (c_P - c_O)c_a}{c_a^2 + r_a^2}\,, \quad L = \frac{R_{LED}^2 - (r_O - r_P)^2 - (c_P - c_O)^2}{c_a^2 + r_a^2}\,. \tag{41}$$

In the examined videos, K is always negative (due to the nearly vertical vibration, i.e., $|r_a| \ll |c_a|$), and the pendulum avoids positions near $\varphi \approx \pm\frac{\pi}{2}$. Hence, only the solution

$$h = -K - \sqrt{L + K^2} \tag{42}$$

is admissible. The coordinate transformation is, therefore, given by

$$h = -K - \sqrt{L + K^2}\,, \tag{43}$$

$$\varphi = -\arcsin\left(\frac{c_P - c_O - h\, c_a}{R_{LED}}\right)\,, \quad \varphi \in \left[-\frac{\pi}{2}, \frac{\pi}{2}\right]\,. \tag{44}$$

For clarity, the diagrams depict φ in the opposite (clockwise) direction.

4.3. Extraction of the slow motion

The coordinate transformation from Section 4.2 is applied to all n pixels belonging to the LED's blurred trajectory (i.e., the connected regions identified in Section 4.1). To estimate the slow motion, represented by φ_0, a single pendulum position is assigned to each frame such that the resulting sequence is smooth, which is achieved by computing a weighted average of the pixel values $\varphi_i,\ i = 1, \dots, n$, with their intensities $I_i,\ i = 1, \dots, n$ as weights:

$$\varphi_0 \approx \frac{\sum_i \varphi_i\, I_i}{\sum_i I_i}\,. \tag{45}$$

This value approximates the expected pendulum position during the exposure, as the weights $I_i / \sum_i I_i$ serve as a numerical approximation of a probability density function.
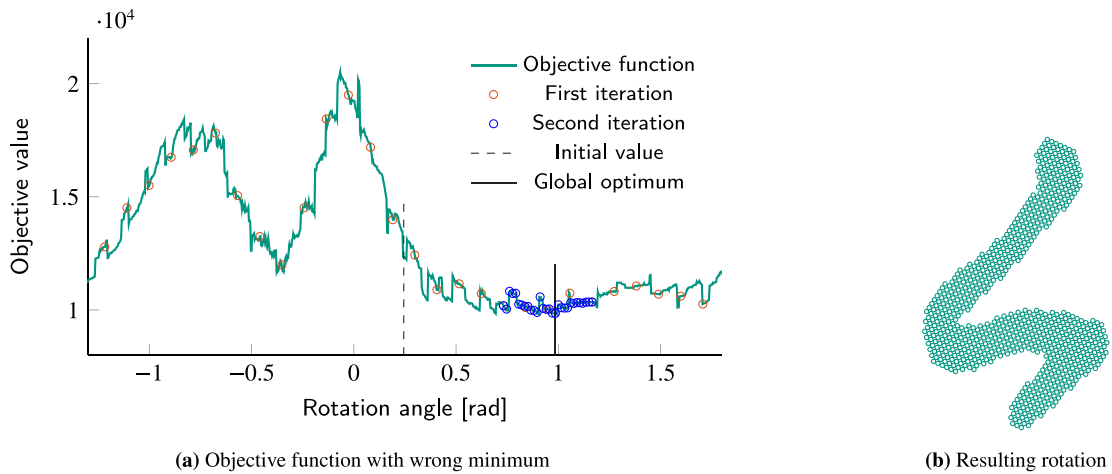
(a) Objective function with wrong minimum

(b) Resulting rotation

Fig. 12. Incorrect rotation angle found by the algorithm due to no erosion.

Due to the rolling shutter effect, the computed angles for the three LEDs differ slightly (see Section 2.3) because the upper pixel rows capture an earlier moment than the lower ones. Although averaging φ_0 over the three LEDs could increase the data set, it would reduce the effective temporal resolution. Therefore, only the slow motion of the outermost LED is considered.

The temporal derivatives of φ_0 with respect to the dimensionless slow time ϑ

$$\frac{\mathrm{d}\varphi_0}{\mathrm{d}\vartheta} = \frac{1}{\Omega_0}\frac{\mathrm{d}\varphi_0}{\mathrm{d}t}, \tag{46}$$

$$\frac{\mathrm{d}^2\varphi_0}{\mathrm{d}\vartheta^2} = \frac{1}{\Omega_0}\frac{\mathrm{d}}{\mathrm{d}t}\left(\frac{\mathrm{d}\varphi_0}{\mathrm{d}\vartheta}\right), \tag{47}$$

are computed in MATLAB® using the `gradient` function, which employs central differences. The time increment is taken as the duration of one frame, i.e. $1/F$, where F denotes the frame rate.

4.4. Trajectory over one period of the fast vibration

The connected regions from Section 4.1 are the basis for tracking the LED's trajectory. These regions are stored in MATLAB® as a point cloud for each frame. For brightness evaluation, a representative path of the LED's centroid is extracted by first rotating the point clouds to define a clear horizontal axis, yielding a path $r_{\mathrm{rot}}(c_{\mathrm{rot}})$ in the rotated (r, c) coordinate system. The adopted method iteratively tracks the rotated point cloud. The detailed procedure is described in Section 4.4.2. The period limits must be determined since integration over h is performed over one oscillation period of the fast vibration. Along the derived path, the arc length s and its differential $\mathrm{d}s$ are computed, and the coordinate transformation from Section 4.2 is applied to obtain h and its differential $\mathrm{d}h$.

4.4.1. Rotation of the frame

An appropriate rotation yields an unambiguous path, i.e., a function $r_{\mathrm{rot}} = f(c_{\mathrm{rot}})$. One way to obtain an appropriate rotation angle is to formulate and solve an optimization problem for each frame. The optimization problem has a single variable, which is the rotation angle α. To formulate the objective function, the point cloud is divided into N pixel groups by parallel, equidistant stripes. Within each pixel group, the largest vertical distances are determined, squared, and summed, thereby penalizing cases where there are several, ambiguous r coordinates for some pixel columns, c, along one frame's trajectory. To improve the objective function's robustness by making the stripe thinner, and thereby having a sharper, better-defined global minimum, the point cloud is eroded, i.e., its binary mask undergoes morphological erosion, every pixel survives only if the entire structuring element (in our case a disk of a given radius, determined by the trajectory's thickness) fits inside the foreground, so one layer of boundary points is stripped away, decreasing significantly the objective function's value in case of an unambiguous rotation but hardly changing it if the rotated trajectory is ambiguous. Then, the optimization problem is solved for a set of equidistantly distributed initial conditions, and the best global optimum is chosen for the rotation angle. Figs. 12 and 13 illustrate the objective function for a frame, showing the initial angle α_0 (dashed line) and the optimal rotation angle α_f (solid line) along with the rotated point cloud for both the original and eroded data. Fig. 14 represents the rotation process graphically.

The number of strips, N, is determined by the width of the eroded point cloud:

$$N = \mathrm{round}\left(\frac{\max c - \min c}{2}\right). \tag{48}$$

Each strip is approximately two pixels wide, and the optimal α minimizes the sum of the squared vertical extents within these strips. The final rotation angle α_f is applied to the complete point cloud and used in Section 4.4.2 for subsequent path tracking.
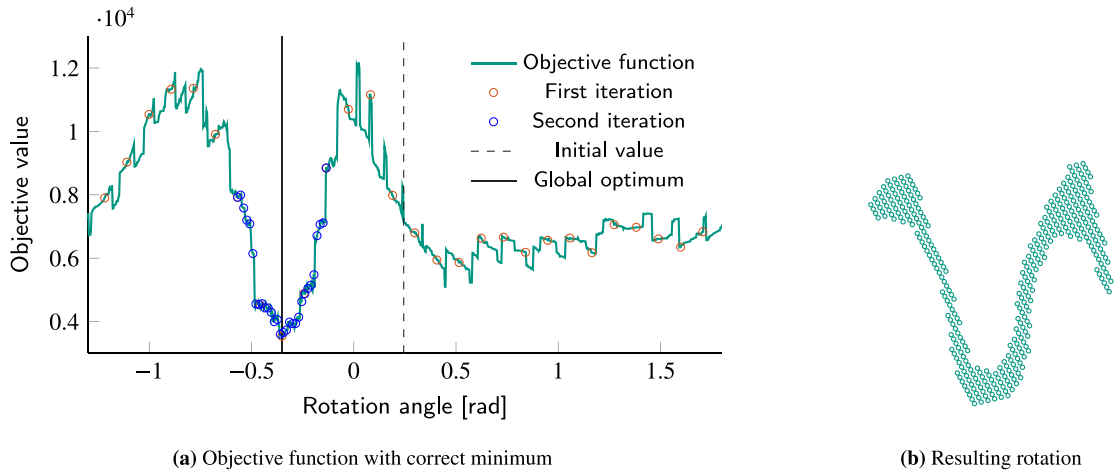
(a) Objective function with correct minimum

(b) Resulting rotation

Fig. 13. Correct rotation angle found by the algorithm after erosion.

(a) Point cloud

(b) Eroded point cloud

(c) Division into strips

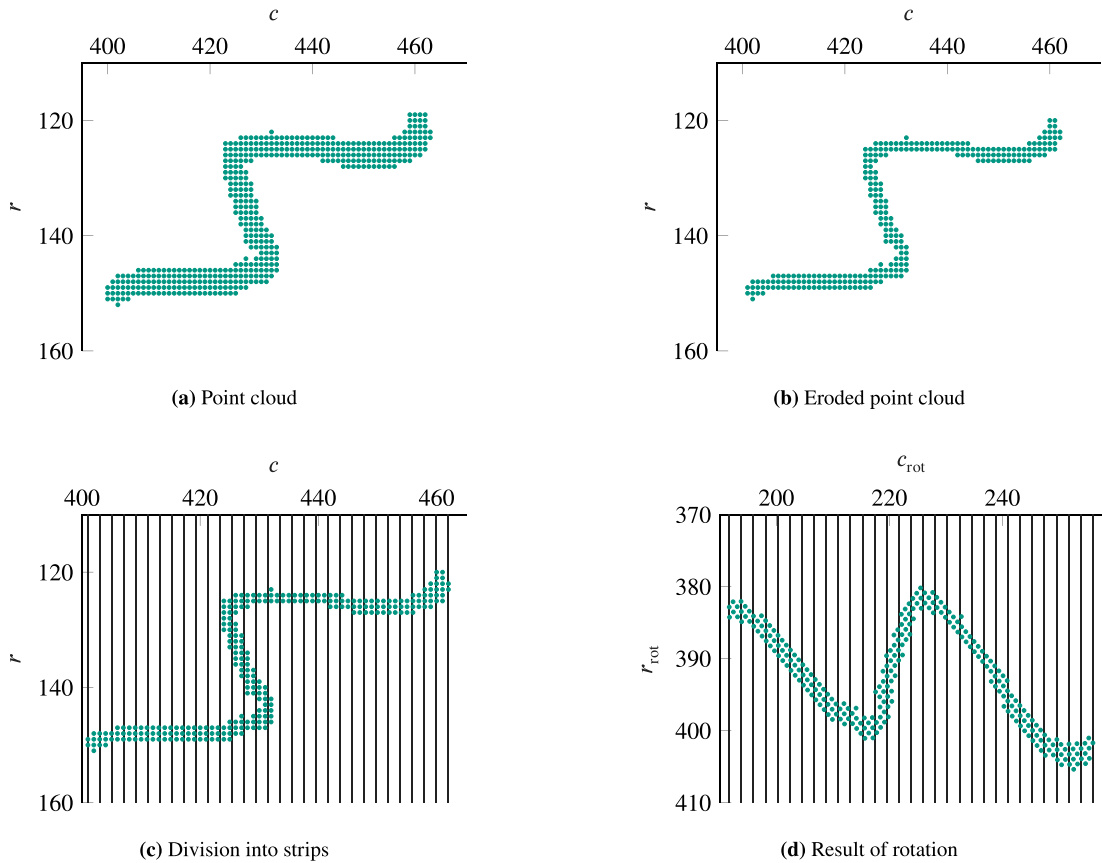

(d) Result of rotation

Fig. 14. Rotation process. Panel (a) displays the original point cloud, panel (b) the eroded point cloud (obtained using a circular structuring element with a radius chosen according to the LED-to-camera distance), panel (c) the division of the eroded point cloud into strips, and panel (d) the final rotation angle.

4.4.2. Path tracking

The path-tracking procedure extracts a representative trajectory from the rotated point cloud (see Fig. 15(a)). First, the region defined by the point cloud is established (see Fig. 15(b)), and its leftmost point is selected as the starting position. At each iteration, a candidate point is determined at a fixed distance l from the previous point by maximizing the radius of an inscribed circle within

(a) Rotated point cloud

(b) Filled area

(c) Iterative path tracking $i = 4$

(d) Iterative path tracking $i = 50$
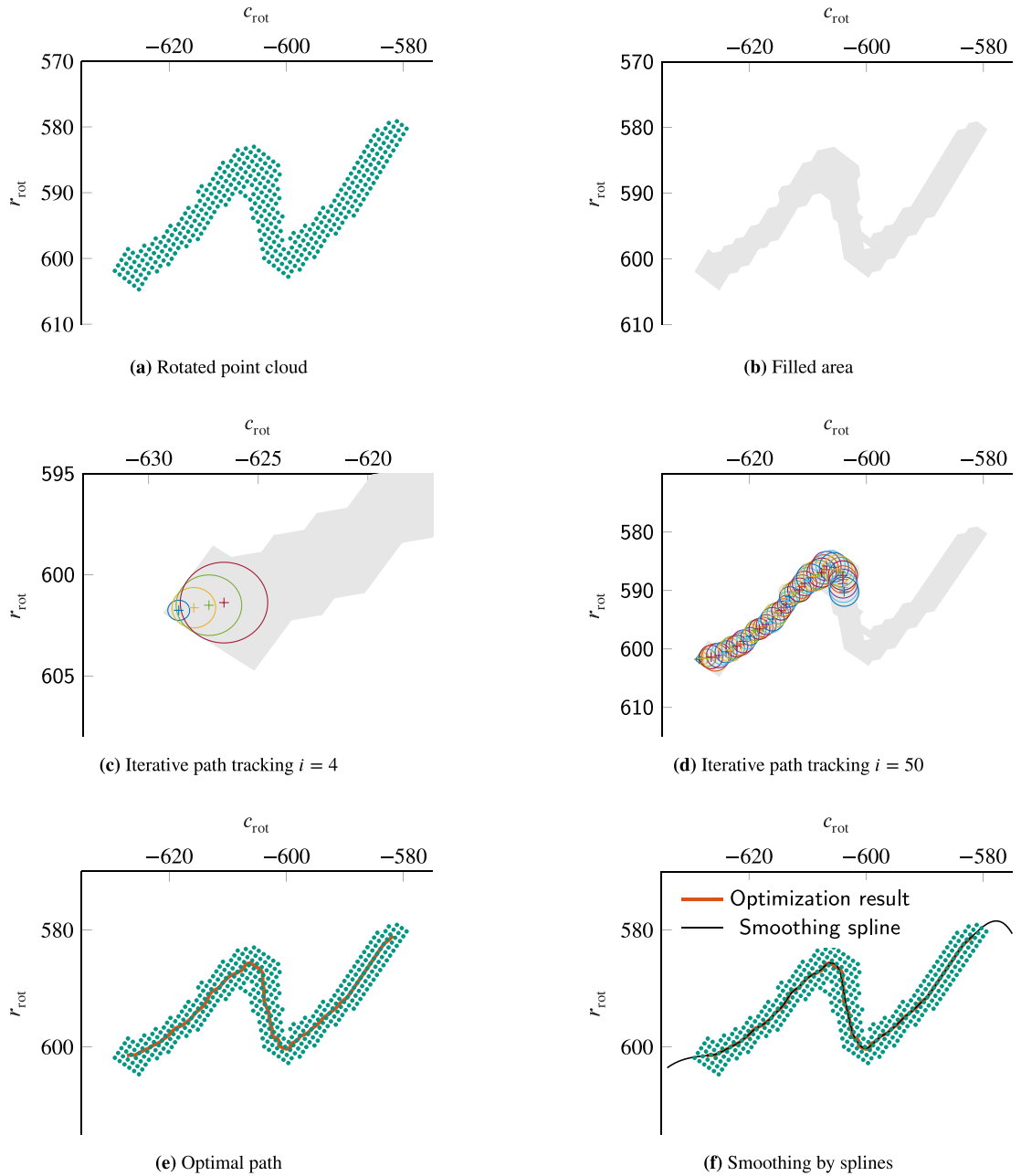
(e) Optimal path

(f) Smoothing by splines

Fig. 15. Illustration of the path tracking.

the region (see Fig. 15(c)). The search is constrained by an upper bound on the radius to ensure stability near turning points; in cases with multiple candidates, spatial criteria are used to resolve ambiguities (see Fig. 15(d)).

The iteration terminates when the candidate circle's radius falls below a predefined minimum. The first and last three points are discarded to avoid edge effects, resulting in the final tracked path (see Fig. 15(e)). The parameters l, the maximum, and the minimum radius are calibrated based on the apparent LED size in the image. In this study, satisfactory results were obtained with $l = 0.7$ pixels, a maximum radius of 2.5 pixels, and a minimum radius equal to l. Frames yielding paths shorter than a minimum length determined by the amplitude and l are discarded. Finally, usable paths are smoothed using a spline with a smoothing parameter of 0.9 (see Fig. 15(f)).

4.4.3. Extracting quantities for one period of the fast vibration

The smoothed path is truncated accordingly to evaluate the average integral in Eq. (87) over one vibration period of the fast vibration. First, 150 points are sampled along the spline and transformed back to the original (r, c) coordinate system to find the values of h. Then, a period is defined by selecting the first point for which $-0.9 < h < 0.9$ and, via linear interpolation, the subsequent point where h repeats this value. Then, the spline between these two points is resampled at $n = 1000$ points and transformed back into (r, c) coordinates. Finite differences approximate the derivative:

$$\frac{\mathrm{d}h}{\mathrm{d}s} \approx \frac{\Delta h}{\Delta s}, \tag{49}$$

with

$$(\Delta h)_i = h_{i+1} - h_i, \qquad i = 1, \dots, n, \tag{50}$$

$$(\Delta s)_i = \sqrt{(r_{i+1} - r_i)^2 + (c_{i+1} - c_i)^2}, \quad i = 1, \dots, n. \tag{51}$$

4.5. CPD and integration along the path

The CPD along the path is derived from the incident light intensity. Under constant LED flux and unambiguous motion, the recorded intensity I is proportional to the incident light I_0 and, by Eq. (85), to the CPD:

$$\rho \sim \frac{1}{v} \sim I_0 \sim I. \tag{52}$$

Normalization,

$$1 = \int_{s_1}^{s_2} \rho(\tilde{s}) \mathrm{d}\tilde{s} = \frac{\rho}{I} \int_{s_1}^{s_2} I(\tilde{s}) \mathrm{d}\tilde{s}, \tag{53}$$

implies that

$$\rho(s) = \frac{I(s)}{\int_{s_1}^{s_2} I(\tilde{s}) \mathrm{d}\tilde{s}}, \quad s \in [s_1, s_2]. \tag{54}$$

Since the intensity is known only at discrete pixels, $I(s)$ is interpolated linearly on the two-dimensional brightness grid at the n points along the path, and trapezoidal integration is employed for both normalization and subsequent evaluations in Eq. (87).

4.6. Angular frequency

The angular frequency Ω is estimated from the zero crossings of h. 150 sampled points from the transformed path are used to count the number of sign changes N_0 over N_F frames. Since two zero crossings correspond to one period, the angular frequency is approximated by

$$\Omega = 2\pi \frac{N_0}{2} \frac{F}{N_F}, \tag{55}$$

with F denoting the frame rate.

4.7. Vibration-induced potential

The vibration-induced potential (see Section 3.3) is computed using the moment of inertia J_S, the total mass m_{tot}, the center-of-mass position R_S, and a scaling factor relating pixel dimensions to physical lengths. The values are computed using the measured properties described in Table 1. The total mass is

$$m_{tot} = m_{Rod} + m_{KL}. \tag{56}$$

The center-of-mass position is given by

$$R_S = \frac{m_{KL}}{m_{tot}} R_{S,KL} + \frac{m_{Rod}}{m_{tot}} R_{S,Rod}, \tag{57}$$

with

$$R_{S,KL} = 0, \quad \text{and} \quad R_{Rod} = R_a + \frac{l_{Rod}}{2}, \tag{58}$$

so that

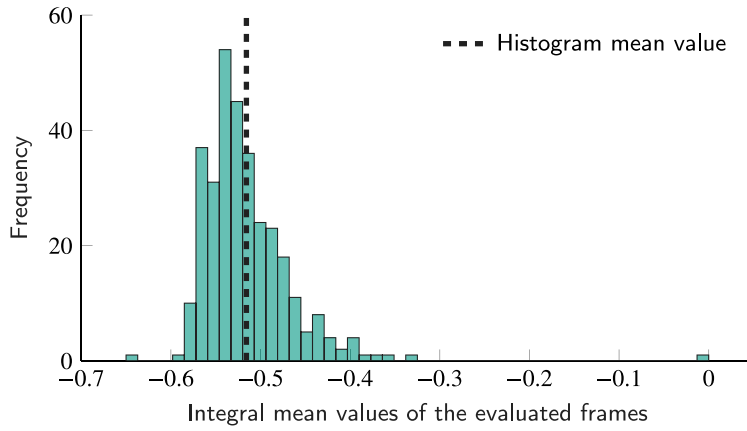$$R_S = \frac{m_{Rod}}{m_{tot}} \left(R_a + \frac{l_{Rod}}{2} \right). \tag{59}$$

Fig. 16. Histogram of the frame-wise mean values. The vertical line indicates the arithmetic average of −0.5157.

The moment of inertia about S is determined via the parallel-axis theorem:

$$
\begin{aligned}
J_S &= J_{S,\text{Rod}} + J_{S,\text{KL}} \\
&= m_{\text{Rod}}\left(\frac{l_{\text{Rod}}^2}{12} + \left(\frac{l_{\text{Rod}}}{2} + R_a - R_S\right)^2\right) + m_{\text{KL}}\left(\frac{R_i^2 + R_a^2}{2} + R_S^2\right).
\end{aligned}
\tag{60}
$$

A scaling factor is computed as the mean of the ratios between the measured distances $R_{\text{LED,i}}$ (and the amplitude $|\vec{a}|$) and the corresponding image-derived values (see Section 4.1). This factor enables the determination of the amplitude vector components x_a and y_a. With the constants from Eq. (22), the vibration-induced potential (Eq. (28)) is calculated using the averaged result from Section 4.5.

5. Results and discussion

5.1. Averaging

The temporal average necessary to determine the vibration-induced potential and describe the slow motion φ_0 (cf. Eq. (24)) was computed from video data using the CPD based on the procedure outlined in Section 4. The analysis assumes high-frequency excitation ($\Omega \gg \Omega_0$), negligible damping, and a linear relation between the recorded intensity and the incident light. Under these conditions, the average can be derived solely from the video data. Fig. 16 shows the distribution of frame-wise means and their overall average.

For a sinusoidal excitation, e.g. $f(\Omega t) = \sin \Omega t$, the expected mean value is

$$
\left\langle \frac{d^2 \sin(\tau)}{d\tau^2} \sin(\tau) \right\rangle_\tau = \frac{1}{2\pi} \int_0^{2\pi} -\sin^2(\tau)\, d\tau = -\frac{1}{2},
\tag{61}
$$

which is slightly lower in magnitude than the measured average −0.5157. This discrepancy may stem from uncertainties in estimating the radii, amplitudes, and trajectory.

5.2. Approximation of the slow motion

The slow variable φ_0 is then determined for each frame as light-intensity-weighted average along the splines. An example is shown in Fig. 17.

For the slow system's identification, the following simple nonlinear model was used based on the truncated Taylor expansion of a symmetric, unknown potential

$$
\ddot{\varphi} + d_1 \dot{\varphi} + c_1(\varphi - B) - c_3(\varphi - B)^3 + c_5(\varphi - B)^5 = 0.
\tag{62}
$$

From the video data values for $\varphi(t_n)$ were obtained and numerical derivatives $\dot{\varphi}(t_n)$, and $\ddot{\varphi}(t_n)$ were calculated using dimensional time t. Notably, the data $\varphi(t_n)$ were smooth enough not to have significant noise even after two-fold numerical differentiation. Table 2 lists the fitted parameters, and Fig. 18 shows the surface fit in the three-dimensional phase space along with the measured data points. A standard Gaussian least-squares fit was implemented. However, the confidence intervals should be interpreted with caution as the conditions for such a fit are not necessarily fulfilled. The identified parameter values are consistent with preliminary estimates and indicate negligible damping (as evidenced by the small value of d_1).
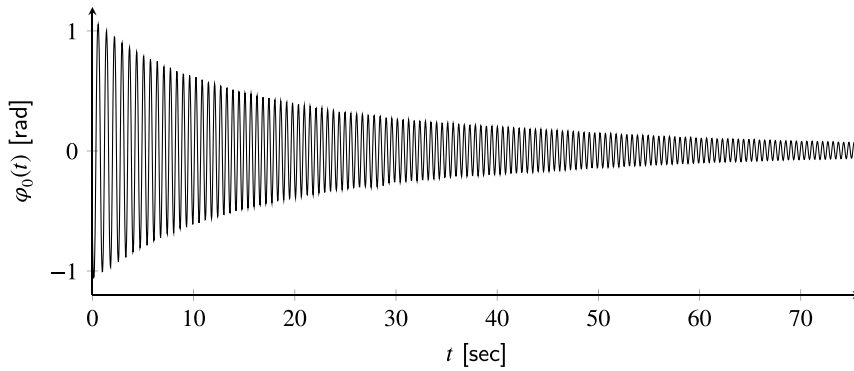
Fig. 17. Time evolution of the light-intensity-weighted average angle against the physical time t.
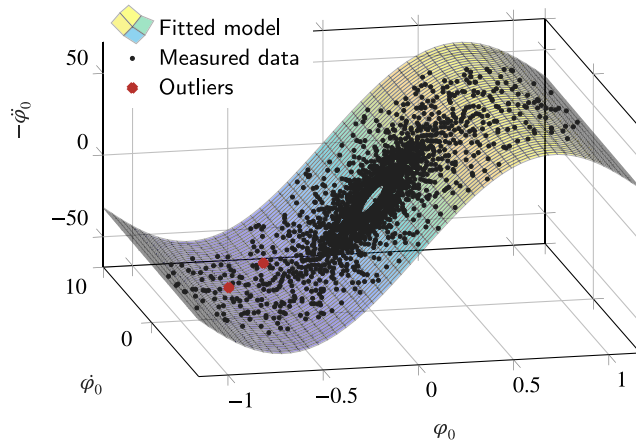

Fig. 18. Model fit to the slow motion obtained from video data.

Table 2
Fitted model parameters with 95% confidence intervals.

Parameter	Value	Lower bound	Upper bound
B	0.0061	0.0055	0.0067
c_1	124.9829	124.4556	125.5102
c_3	101.2335	98.6122	103.8548
c_5	21.8904	19.3714	24.4093
d_1	0.0808	0.0562	0.1054

5.3. Vibration-induced potential and approximation of the unexcited system

The potential for the slow motion and the angular frequency Ω are computed from the averaged video data, the pendulum position φ_0, and constants a and b, which also rely on measured quantities (Table 1) according to Eq. (22) resulting in

$$\Omega = 303.6592, \qquad \Omega_0 = 6.8849, \qquad a = -0.093, \qquad b = 2.5484. \tag{63}$$

The unexcited system's potential is estimated by

$$U_{0,\text{approx}}(\varphi_0) = \int \ddot{\varphi}_0 \, d\varphi_0 - U_{V,\text{approx}}(\varphi_0). \tag{64}$$

Fig. 19 compares the potential derived from the video data with the analytically computed sinusoidal potential $U_{V,\text{sin}}$ and the gravitational potential $U_{0,g}$ over the integration interval $[\varphi_{0,\text{min}}, \varphi_{0,\text{max}}]$ determined by the maximal vibration range on the experimental recording. The potentials exhibit similar shapes, although a slight rightward shift of the equilibrium and differences in magnitude are observed, which may be due to the non-perfectly vertical motion of the suspension point ($a \neq 0$).
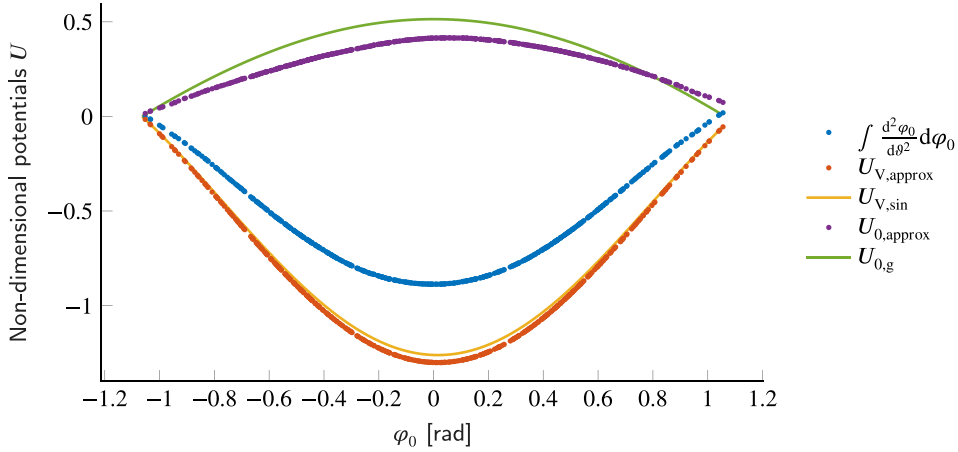
Fig. 19. Comparison of the vibration-induced potential $U_{V,approx}$ with the sinusoidal potential $U_{V,sin}$ and the gravitational potential $U_{0,g}$, as well as the restored gravitational potential $U_{0,approx}$ based only on video data. The restoration is possible in the range $[\varphi_{0,min}, \varphi_{0,max}]$, where vibration data is recorded.
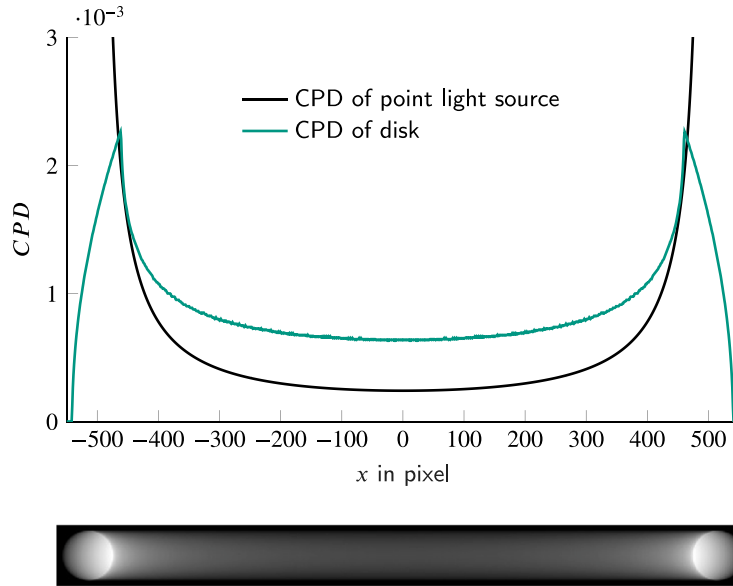

Fig. 20. Comparison of the brightness distribution of a white disk on a black background with the CPD of the center position.

5.4. Description of possible error sources

The transformation from pixel coordinates (r, c) to the physical variables h and the pendulum angle φ (see Section 4.2) is based on calibrating the LED position along the rod, R_{LED}, the turning points of the suspension motion A_t and A_b, and the reference origin O (cf. Eq. (40)). These calibration values are derived from the video data using the procedure described in Section 4.1. A central assumption is that the intensity maximum in each frame represents the LED's center when it momentarily slows down at turning points. However, because the LED has a finite size spanning several pixels, the recorded intensity maximum is shifted inward relative to the actual center of the LED. This effect is demonstrated in Fig. 20, where a simulated frame from MATLAB® – with the LED modeled as a white disk sampled 255 times during one exposure – shows that the peak intensity does not align with the true center but is offset toward the interior of the curvature. The trajectory approximation in Section 4.4 does not incorporate intensity information, which results in misalignment and leads to nonphysical values (e.g., $|h| > 1$) and overestimates both h and its derivative h'. These inaccuracies, in turn, affect the computed pendulum angle φ. Moreover, variations in amplitude and curvature radii influence the scaling factor used in Section 4.7 to determine the parameters a and b of the vibration-induced potential.

Additional uncertainties arise from the experimental setup. The camera is manually aligned using a tripod, which may not ensure perfect perpendicularity to the image plane, and manual measurements of quantities such as mass and length inherently
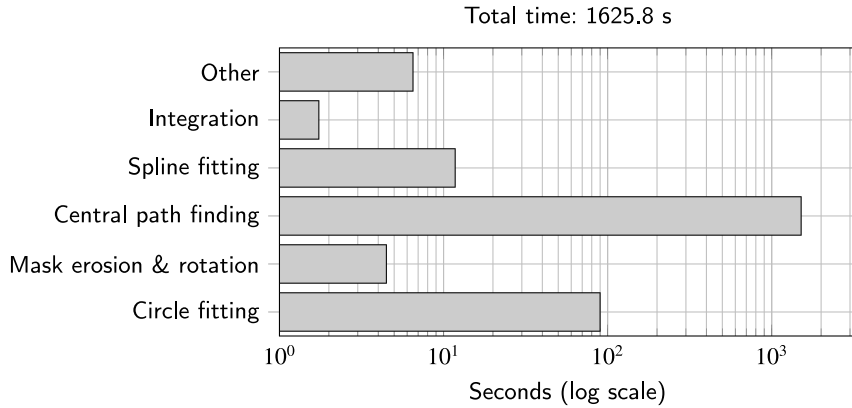
Fig. 21. Computational time distribution.

carry inaccuracies. Simplifications in modeling the pendulum, such as assuming a continuous mass distribution while neglecting the discrete contributions of the LED, its cables, and the internal structure of the ball bearing, further increase the overall error. Errors in determining the CPD can also be significant. Because the LED is not point-like, its recorded brightness distribution deviates from the ideal CPD that would result from a Dirac delta function.

Finally, the estimation of the angular frequency Ω, obtained by counting the zero crossings in h, is subject to error due to the exclusion of frames at the pendulum's extreme positions and potential fluctuations in the motor's frequency during recording. The use of several adjustable parameters in the video analysis further affects the accuracy of the determined trajectory and the final results.

5.5. Other aspects

The computational time for different parts of the code is shown in Fig. 21. For the evaluation, a single core of a Lenovo Thinkpad with Intel® Core™ i5-10210U processor at 1.6 GHz was used. By far the slowest step is determining the central path of the LED trajectories in each frame. This routine was written with robustness in mind, not speed, so substantial optimization potential remains.

In addition to the Canon Powershot G7 X camera, a Raspberry Pi Camera Module 3 (costing 28,90 €) with full HD video quality at 30 FPS was also tested. The video quality turned out to be equally good as that of the much more expensive Canon camera. For the comparison of results between the Canon Powershot G7 X, the Raspberry Pi camera, and the camera of a Samsung Galaxy S23 mobile phone, videos can be found under the links specified in the Data availability section.

The proposed method is strictly marker-based: point-like LEDs are used because they dominate the image, so background suppression and feature tracking are unnecessary. Replacing the LED markers with a continuous surface whose light intensity does not differ significantly from its background would completely change the problem. To subtract the light intensity information and obtain the CPD, new algorithms need to be implemented, which is undoubtedly an interesting future research direction. A computationally heavier pipeline that we have not explored; assessing it lies outside the scope of the present work and is left for future study. However, for more flexibility, a wireless LED marker was designed (see Fig. 22(a)). Also the application of a LED strip is thinkable for such continuous analysis (see Fig. 22(b)).

6. Conclusion and outlook

This work has demonstrated that the classical probability density hidden in long-exposure frames is sufficient to perform experimental averaging on a fast–slow mechanical system. We derived the slow-flow equations for a Kapitza pendulum directly from video data, recovered the vibration-induced potential, and even reconstructed the underlying gravitational potential in the range covered by the experiment. All measurements were taken using pocket-sized hardware, including three battery-powered LEDs and a consumer-grade camera. The results confirm that long-exposure imaging, coupled with a straightforward image-processing pipeline, delivers the same dynamical insight that would typically require a high-speed camera and heavy numerical integration.

The implications reach well beyond the pendulum. Practical application examples include model identification and data-driven model building for high-frequency–excited machinery—such as vibratory rammers, vibrating energy harvesters, tuned-mass dampers, vibratory conveyors, vibrating screens, and even self-synchronizing unbalanced motors. Because the method extracts the slow dynamics without requiring time-resolved data, it significantly decreases storage and bandwidth costs. At a few euros per LED, a grid of blur-based probes could monitor large structures where accelerometers or lasers are too costly or intrusive. Combining the blur-derived CPD with FFT-based convolution further accelerates the averaging step, opening up real-time applications such as feedback control or online parameter identification.

(a) Wireless, 3D-printed LED marker with in-built potentiometer
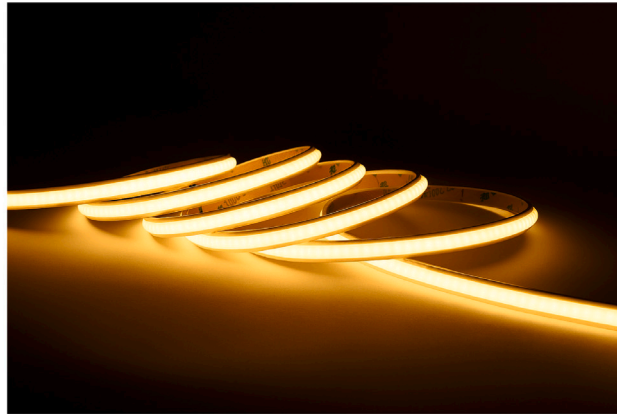
(b) Continuous LED strip for 1D continuum slow–fast vibrational problems

Fig. 22. Different LED concepts for distributed and continuous CPD-based measurements.

A natural next step is to invert the problem entirely: instead of reducing blur to a probability density, recover the entire time history from a single streak. Under mild assumptions — continuity, differentiability, and bounded acceleration — the most probable trajectory could be estimated with Bayesian or variational techniques. Early work on photosequencing already hints at this possibility. Success there would turn every blurred snapshot into a compressed recording of continuous time-series data, pushing low-cost, lens-based metrology into domains now served only by specialized high-speed systems.

CRediT authorship contribution statement

Attila Genda: Writing – review & editing, Writing – original draft, Visualization, Validation, Supervision, Methodology, Investigation, Formal analysis, Conceptualization. **Clemens Kummer:** Writing – review & editing, Visualization, Validation, Software, Investigation, Formal analysis, Data curation. **Alexander Fidlin:** Writing – review & editing, Supervision, Resources, Project administration, Funding acquisition, Conceptualization.

Declaration of competing interest

The authors declare that they have no known competing financial interests or personal relationships that could have appeared to influence the work reported in this paper.

Acknowledgments

Appendix A. Multiple-scales derivation

This appendix gives the derivation of the slow-flow equations using the method of multiple scales. The starting point is the equation of motion (23). Assuming an asymptotic expansion

$$\varphi(\vartheta, \tau) = \varphi_0(\vartheta, \tau) + \frac{1}{\omega}\varphi_1(\vartheta, \tau) + \frac{1}{\omega^2}\varphi_2(\vartheta, \tau) + \dots , \tag{65}$$

with the functions $\varphi_0, \varphi_1, \varphi_2, \dots$ being periodic and bounded in τ, we use the small-angle approximations

$$\cos \gamma \approx 1 \quad , \quad \sin \gamma \approx \gamma \quad \text{for} \quad \gamma = \mathcal{O}\left(\frac{1}{\omega}\right) \tag{66}$$

to obtain:

$$\sin \varphi \approx \sin \varphi_0 + \frac{1}{\omega}\varphi_1 \cos \varphi_0 , \tag{67}$$

$$\cos \varphi \approx \cos \varphi_0 - \frac{1}{\omega}\varphi_1 \sin \varphi_0 . \tag{68}$$

Inserting Eqs. (67)–(68) into Eq. (23) and collecting terms by powers of ω up to magnitude $\mathcal{O}(\omega^0)$, we obtain:

$$\mathcal{O}(\omega^2): \quad \omega^2 \frac{\partial^2 \varphi_0}{\partial \tau^2} = 0, \tag{69}$$

$$\mathcal{O}(\omega^1): \quad 2\omega \frac{\partial^2 \varphi_0}{\partial \vartheta \partial \tau} + \omega \frac{\partial^2 \varphi_1}{\partial \tau^2} = \omega \frac{d^2 f(\tau)}{d\tau^2} \left(a \cos \varphi_0 + b \sin \varphi_0 \right), \tag{70}$$

$$\mathcal{O}(\omega^0): \quad \frac{\partial^2 \varphi_0}{\partial \vartheta^2} + 2 \frac{\partial^2 \varphi_1}{\partial \vartheta \partial \tau} + \frac{\partial^2 \varphi_2}{\partial \tau^2} = \frac{d^2 f(\tau)}{d\tau^2} \varphi_1 \left(-a \sin \varphi_0 + b \cos \varphi_0 \right) + \sin \varphi_0 - \omega\delta \frac{\partial \varphi_0}{\partial \tau}. \tag{71}$$

Eqs. (69)–(71) can be solved iteratively. From Eq. (69), double integration yields

$$\varphi_0 = A(\vartheta) \tau + B(\vartheta), \tag{72}$$

and boundedness in τ requires $A(\vartheta) = 0$, so that

$$\varphi_0 = B(\vartheta). \tag{73}$$

Thus, φ_0 depends only on the slow time ϑ. Next, from Eq. (70) we obtain

$$\varphi_1 = f(\tau) \left(a \cos \varphi_0 + b \sin \varphi_0 \right) + D(\vartheta), \tag{74}$$

where any term growing linearly in τ is discarded to ensure boundedness. Averaging the $\mathcal{O}(\omega^0)$ equation in the fast time τ over one period (which eliminates τ-derivative terms of periodic functions) then yields an equation for the slow dynamics:

$$\frac{d^2 \varphi_0}{d\vartheta^2} = \left[\frac{b^2 - a^2}{2} \sin 2\varphi_0 + ab \cos 2\varphi_0 \right] \left\langle \frac{d^2 f(\tau)}{d\tau^2} f(\tau) \right\rangle_\tau + \sin \varphi_0. \tag{75}$$

Here, the first term represents the vibration-induced contribution, while the second term arises from the gravitational force.

Appendix B. Video-compatible transformation of the averaged term

The goal is to approximate the average

$$\left\langle \frac{d^2 f(\tau)}{d\tau^2} f(\tau) \right\rangle_\tau = \frac{1}{\tau_2 - \tau_1} \int_{\tau_1}^{\tau_2} \frac{d^2 f(\tau)}{d\tau^2} f(\tau) \, d\tau, \tag{76}$$

where τ_1 and τ_2 span one period of f. Because differentiating twice can introduce numerical errors, we perform integration by parts:

$$\left\langle \frac{d^2 f(\tau)}{d\tau^2} f(\tau) \right\rangle_\tau = \frac{1}{\tau_2 - \tau_1} \left[\frac{df(\tau)}{d\tau} f(\tau) \right]_{\tau_1}^{\tau_2} - \frac{1}{\tau_2 - \tau_1} \int_{\tau_1}^{\tau_2} \left(\frac{df(\tau)}{d\tau} \right)^2 d\tau. \tag{77}$$

Since f is periodic, the boundary term vanishes.

A substitution is then introduced by relating the fast time τ to the arc length s along the trajectory of the point P_{LED}:

$$\tau = g(s), \quad d\tau = g'(s) \, ds. \tag{78}$$

With this change of variable, the average becomes

$$\left\langle \frac{d^2 f(\tau)}{d\tau^2} f(\tau) \right\rangle_\tau = -\frac{1}{\tau_2 - \tau_1} \int_{s_1}^{s_2} \left(\frac{df(g(s))}{d\tau} \right)^2 g'(s) \, ds = -\frac{1}{\Omega(\tau_2 - \tau_1)} \int_{s_1}^{s_2} \left(\frac{dh}{ds} \right)^2 v(s) \, ds, \tag{79}$$

where the speed along the arc is defined as

$$v(s) = \frac{ds}{dt} = \Omega \frac{ds}{d\tau}. \tag{80}$$

Since the fast time period satisfies $\tau_2 - \tau_1 = \Omega T$ with $T = \frac{2\pi}{\Omega}$, the above expression becomes

$$\left\langle \frac{d^2 f(\tau)}{d\tau^2} f(\tau) \right\rangle_\tau = -\frac{1}{2\pi\Omega} \int_{s_1}^{s_2} \left(\frac{dh}{ds} \right)^2 v(s) \, ds. \tag{81}$$

B.1. Connection to the classical probability density

The probability that a continuous function $\xi(t)$ takes a value in the interval $[a, b]$ can be written in terms of its CPD ρ_ξ as

$$P(\xi \in [a, b]) = \int_a^b \rho_\xi(\eta) \, d\eta. \tag{82}$$

Since the total probability must be one,

$$\int_{-\infty}^{\infty} \rho_\xi(\eta) \, d\eta = 1. \tag{83}$$

For the point P_{LED} moving along the arc, the infinitesimal time spent in the interval $[s, s + \mathrm{d}s]$ is

$$\mathrm{d}t = \frac{\mathrm{d}s}{v(s)}, \tag{84}$$

so that the probability of finding the point in $[s, s + \mathrm{d}s]$ is

$$\rho(s)\mathrm{d}s = \frac{\mathrm{d}t}{T_s} = \frac{1}{T_s}\frac{\mathrm{d}s}{v(s)}, \tag{85}$$

with T_s being the total time along the arc. For one period $T = \frac{2\pi}{\Omega}$ of $f(\Omega t)$, the CPD is given by

$$\rho_T(s) = \begin{cases} \dfrac{1}{T}\dfrac{1}{v(s)} & s \in [s_1, s_2], \\ 0 & \text{otherwise}. \end{cases} \tag{86}$$

Using this relation, the average in Eq. (79) can be rewritten as

$$-\frac{1}{2\pi\Omega}\int_{s_1}^{s_2}\left(\frac{\mathrm{d}h}{\mathrm{d}s}\right)^2 v(s)\,\mathrm{d}s = -\frac{1}{4\pi^2}\int_{s_1}^{s_2}\left(\frac{\mathrm{d}h}{\mathrm{d}s}\right)^2\frac{1}{\rho_T(s)}\,\mathrm{d}s. \tag{87}$$

Thus, the complete averaged equation for the slow dynamics becomes

$$\frac{\mathrm{d}^2\varphi_0}{\mathrm{d}\vartheta^2} = -\left(\frac{b^2 - a^2}{2}\sin 2\varphi_0 + ab\cos 2\varphi_0\right)\frac{1}{4\pi^2}\int_{s_1}^{s_2}\left(\frac{\mathrm{d}h}{\mathrm{d}s}\right)^2\frac{1}{\rho_T(s)}\,\mathrm{d}s + \sin\varphi_0. \tag{88}$$

Data availability

Video data is available for Raspberry Pi and cell phone footage under this and this link. The Canon Powershot G7 X camera recordings, as well as a technical drawing of the Kapitza pendulum, are available at this link.

References

[1] Joseph-Louis Lagrange, Mécanique Analytique, vol. 2, La Veuve Desaint, Paris, 1789.
[2] Henri Poincare, Les methodes nouvelles de la mecanique celeste, vol. I–III, Gauthier-Villars, Paris, 1892.
[3] B. van der Pol, A theory of the amplitude of free and forced triode vibrations, Radio Rev. 1 (1920) 701–710, 754–762.
[4] Pierre Fatou, Sur le mouvement d'un système soumis à des forces à courte période, Bull. Soc. Math. Fr. 56 (1928) 98–139.
[5] N.M. Krylov, N.N. Bogoliubov, New Methods of Nonlinear Mechanics in their Application to the Investigation of the Operation of Electronic Generators, I (in Russian), United Scientific and Technical Press, Moscow, 1934.
[6] Nicolai M. Krylov, Nikolai N. Bogoliubov, Introduction to Nonlinear Mechanics, Princeton University Press, Princeton, NJ, 1943, Transl. of 1937 Russian edition; see also French edition: Méthodes approchées de la mécanique non linéaire dans leurs applications, Acad. Sci. Ukraine, 1935.
[7] N.N. Bogoliubov, Y.A. Mitropolsky, Asymptotic Methods in the Theory of Non-Linear Oscillations, Gordon & Breach, New York, 1961.
[8] A.R.E. Oliveira, History of Krylov-Bogoliubov-Mitropolsky methods of nonlinear oscillations, Adv. Hist. Stud. 6 (2017) 40–55.
[9] Jason J. Bramburger, Daniel Dylewsky, J. Nathan Kutz, Sparse identification of slow timescale dynamics, Phys. Rev. E 102 (2) (2020) 022204.
[10] Chihiro Hayashi, Nonlinear Oscillations in Physical Systems, McGraw-Hill, New York, 1964.
[11] Ali H. Nayfeh, Perturbation Methods, John Wiley & Sons, New York, 1973.
[12] J.A. Sanders, F. Verhulst, J. Murdock, Averaging methods in nonlinear dynamical systems, in: Applied Mathematical Sciences, Springer New York, New York, NY, 2007.
[13] Alexander Fidlin, Nonlinear oscillations in mechanical engineering, Springer Science & Business Media, Heidelberg, 2005.
[14] Ali H. Nayfeh, Dean T. Mook, Nonlinear Oscillations, John Wiley & Sons, New York, 1979.
[15] John Guckenheimer, Philip Holmes, Nonlinear oscillations, dynamical systems, and bifurcations of vector fields, Applied Mathematical Sciences, 42, Springer, New York, 1983.
[16] Attila Genda, Alexander Fidlin, Oleg Gendelman, An alternative approach to averaging in nonlinear systems using classical probability density, ZAMM - J. Appl. Math. Mech. / Z. Angew. Math. Mech. 104 (6) (2024) e202300432.
[17] Attila Genda, Alexander Fidlin, Oleg Gendelman, Model reduction for an internally damped n-particle chain in a potential well under polyharmonic excitation, Acta Mech. 235 (7) (2024) 4669–4692.
[18] R.L. Stratonovich, Topics in the Theory of Random Noise, vol. 1, Gordon and Breach, New York, 1963.
[19] R.Z. Khasminskii, A limit theorem for the solutions of differential equations with random right-hand sides, Theory Probab. Appl. 11 (3) (1966) 390–406.
[20] G.C. Papanicolaou, W. Kohler, Asymptotic theory of mixing stochastic ordinary differential equations, Commun. Pure Appl. Math. 27 (1974) 641–668.
[21] Daniel T. Bartilson, Kyle T. Wieghaus, Stefan Hurlebaus, Target-less computer vision for traffic signal structure vibration studies, Mech. Syst. Signal Process. 60–61 (2015) 571–582.
[22] Justin G. Chen, Abe Davis, Neal Wadhwa, Frédo Durand, William T. Freeman, Oral Büyüköztürk, Video camera–based vibration measurement for civil infrastructure applications, J. Infrastruct. Syst. 23 (3) (2017) 04017025.
[23] Yi-Nan Jeng, Chih-Hsiung Wu, Frequency Identification of Vibration Signals Using Video Camera Image Data, Sensors 12 (10) (2012) 13871–13898.
[24] Hao-Yu Wu, Michael Rubinstein, Eugene Shih, John Guttag, Frédo Durand, William Freeman, Eulerian video magnification for revealing subtle changes in the world, ACM Trans. Graph. 31 (4) (2012).
[25] Kui Luo, Xuan Kong, Jinzhao Li, Jiexuan Hu, Lu Deng, Motion magnification for video-based vibration measurement of civil structures: A review, Mech. Syst. Signal Process. 220 (2024) 111681.
[26] Li Mengzhu, Liu Gang, Mao Zhu, Phased-based motion estimation through short-distance hilbert transform, Mech. Syst. Signal Process. 211 (2024) 111219, https://www.sciencedirect.com/science/article/pii/S0888327024001171.
[27] Yihan Wang, Lahav Lipson, Jia Deng, SEA-RAFT: Simple, efficient, accurate RAFT for optical flow, in: Computer Vision – ECCV 2024 – Lecture Notes in Computer Science, vol. 15065, 2024, pp. 36–54.

[28] T.J. Beberniss, D.A. Ehrhardt, High-speed 3D digital image correlation vibration measurement: Recent advancements and noted limitations, Mech. Syst. Signal Process. 86 (2017) 35–48.

[29] Paolo Neri, Alessandro Paoli, Armando V. Razionale, Ciro Santus, Low-speed camera system for 3D-DIC vibration measurements in the kHz range, Mech. Syst. Signal Process. 162 (2022) 108040.

[30] Paolo Neri, Alessandro Paoli, Armando V. Razionale, Salvatore Barone, Enhanced subpixel sensitivity in 3D-DIC via spline-based correlation map interpolation for vibration measurements, Opt. Laser Technol. 188 (2025) 112958.

[31] Paolo Neri, Augmented-resolution digital image correlation algorithm for vibration measurements, Measurement 231 (2024) 114565.

[32] Dongyang Hu, Chen Wang, Di Li, Weiyu Xu, Xiangchao Zhang, Vibration deformation measurement and defect identification based on time-averaged digital holography, Photonics 12 (4) (2025) 373.

[33] Nicholas A. Valente, Zhu Mao, Christopher Niezrecki, Holistically nested edge detection and particle filtering for subtle vibration extraction, Mech. Syst. Signal Process. 204 (2023) 110753.

[34] Lei Bao, Edward F. Redish, Understanding probabilistic interpretations of physical systems: A prerequisite to learning quantum physics, Am. J. Phys. 70 (3) (2002) 210–217.

[35] Y. Yitzhaky, G. Boshusha, Y. Levy, N.S. Kopeika, Restoration of an image degraded by vibrations using only a single frame, Opt. Eng., Bellingham 39 (8) (2000) 2083–2091.

[36] T. Sieberth, R. Wackrow, J.H. Chandler, Motion blur disturbs – the influence of motion-blurred images in photogrammetry, Photogramm. Rec. 29 (148) (2014) 434–453.

[37] S. Wang, B. Guan, G. Wang, Q. Li, Measurement of sinusoidal vibration from motion blurred images, Pattern Recognit. Lett. 28 (9) (2007) 1029–1040.

[38] Antiopi-Malvina Stamatellou, Anestis I. Kalfas, On the efficiency of a piezoelectric energy harvester under combined aeroelastic and base excitation, Micromachines 12 (8) (2021) 962.

[39] David M.J. McCarthy, Jim H. Chandler, Alessandro Palmeri, Monitoring three-dimensional vibrations in structures using high-resolution motion-blurred imagery, Photogramm. Rec. 32 (158) (2017) 222–240.

[40] Ludovít Kovanic, Lubomír Ambrisko, Daniela Marasová, Peter Blist'an, Tomás Kasanicky, Michal Cehlár, Long-exposure RGB photography with a fixed stand for measuring the trajectory of a dynamic impact device, Sensors 21 (20) (2021) 6818.

[41] Genco Karameşe, Ferit Yardımcı, Ahmet Güllü, Ercan Yüksel, Cem Yalçın, Oral Büyüköztürk, Vision-based dynamic response measurements of structures by using smartphone videos and alternative techniques, Int. J. Struct. Stab. Dyn. 23 (7) (2023).

[42] Huinan Gong, Zhenjie Zhou, Jun Pan, Ming Yang, et al., Image motion-blur mechanism-based measurement method for low-frequency vibration amplitude and direction, IEEE Sens. J. (2024) 1–9.

[43] Xiaoyan Liu, Jie Zhang, Lei Wang, Liang Chen, Micro-vibration analysis of a cooled astronomical CCD camera and its impact on long-exposure imaging, Sensors 24 (3) (2024) 1025.

[44] Vijay Rengarajan, Shuo Zhao, Ruiwen Zhen, John Glotzbach, Hamid Sheikh, Aswin C. Sankaranarayanan, Photosequencing of motion blur using short and long exposures, 2019.

[45] D.J. Ness, Small oscillations of a stable inverted pendulum, Am. J. Phys. 35 (1967) 964.

[46] L. Blitzer, Inverted pendulum, Am. J. Phys. 33 (1965) 1076.

[47] F.M. Phelps, III, J.H. Hunter, Jr., An analytic solution of the inverted pendulum, Am. J. Phys. 33 (1965) 285–295.

[48] H.P. Kalmus, The inverted pendulum, Am. J. Phys. 38 (1970) 874.

[49] R.E. King, The inverted pendulum, Am. J. Phys. 33 (1965) 855.

[50] Mark Levi, Stability of the inverted pendulum–A topological explanation, SIAM Rev. 30 (4) (1988) 639–644.

[51] Charles A. Poynton, Digital Video and HDTV: Algorithms and Interfaces, Morgan Kaufmann, Waltham, MA, 2003, p. 260, 630.